Journal of Fluids and Structures 143 (2026) 104537

Contents lists available at ScienceDirect

Journal of Fluids and Structures

journal homepage: www.elsevier.com/locate/jfs

Numerical simulation of vortex-induced vibration response of a single IEA 10-MW wind turbine blade

Xuepeng Fu *, Ganesh Vijayakumar , Bumseok Lee , Michael Sprague

National Laboratory of the Rockies, Golden, CO, 80401, USA

ARTICLE INFO

Keywords:
Vortex-induced vibration
Wind turbine blade
Computational fluid dynamics

ABSTRACT

Three-dimensional simulation of vortex-induced vibration (VIV) of a single International Energy Agency (IEA) 10-MW reference wind turbine blade with a length of 97.325 m is performed using the ExaWind stack, an open-source suite of codes. This study aims to illustrate the spanwise VIV response characteristics and cross-validate the results with an existing commercial framework. Five near-body meshes and three time steps are selected for the convergence study. To improve computational efficiency, several VIV triggering methods are also compared to shorten the VIV development period. The ExaWind-based VIV simulation strategy for a single IEA 10-MW blade is determined. First, the modal shape is validated against published results. Then, spanwise VIV responses of four blade configurations under a fixed and varied incoming flow velocity are analyzed. Results show that the VIV response is dominated by the first edgewise (second overall) mode. Little first-mode contributions appear near the second-mode node, producing a π phase jump, and a higher harmonics response occurs near the blade root. Rotational degrees of freedom are minor compared with translational motion. The response versus reduced velocity is analyzed, showing a two-branch behavior similar to that of VIV for a bluff cylinder. Across all tested cases, the dominant frequency remains locked to the natural frequency of the second mode with no observed desynchronization. A mild deviation is observed for the case of 90-degree pitch and 310-degree azimuth rotation near a reduced velocity of 6, which will be examined with additional cases in future work. These findings indicate that severe VIV responses can arise under specific configurations and flow conditions, thereby increasing the potential for VIV fatigue damage and requiring greater attention during operation.

1. Introduction

Vortex-induced vibration (VIV) of slender structures has been investigated in ocean and wind engineering for decades, including applications such as marine risers and long-span bridges (Xu et al., 2019; Fu et al., 2022b; Huera-Huarte, 2025). VIV occurs when fluid flows past structures, generating the vortex street that induces nonlinear vibrations in both the in-line and cross-flow directions (Zhao et al., 2023). VIV can lead to fatigue damage and structural failure, which requires appropriate mitigation in applied engineering practice.

The canonical simplified model for studying VIV of flexible structures is a rigid circular cylinder in uniform flow (Feng, 1968; Shen et al., 2025), where the cylinder is allowed to vibrate in the in-line and cross-flow directions. The lock-in phenomenon is identified in bluff cylinder VIV research as the matching of the frequency of the periodic wake vortex mode with the body oscillation

* Corresponding author.
E-mail address: xuepeng.fu@nlr.gov (X. Fu).

https://doi.org/10.1016/j.jfluidstructs.2026.104537
Received 3 November 2025; Received in revised form 4 January 2026; Accepted 13 February 2026
Available online 3 March 2026

frequency (Khalak and Williamson, 1999). The lock-in phenomenon in bluff cylinder systems is strongly influenced by the mass ratio (density ratio between structure and fluid). A lower mass ratio leads to a higher lock-in frequency (Govardhan and Williamson, 2000), and when the mass ratio drops below a critical threshold, the system can exhibit a "resonance forever" behavior with no VIV desynchronization region (Govardhan and Williamson, 2002).

For flexible pipe VIV, the response frequency often locks onto different natural frequencies of various modes (Fu et al., 2022a; Huera-Huarte, 2025). The lock-in phenomenon is the matching of the sectional VIV response frequency and corresponding sectional wake shedding frequency (Bourguet et al., 2013). In addition to lock-in, several other VIV phenomena are observed, including traveling waves (Huera-Huarte, 2006; Duan et al., 2021; Fu et al., 2022b), time sharing (Swithenbank and Larsen, 2012), and phase differences (Fan et al., 2019). These issues have been widely studied for over six decades, and many reviews can be referred to, e.g., Willden and Graham (2001), Williamson and Govardhan (2004), Sarpkaya (2004), Williamson and Govardhan (2008), and Huera-Huarte (2025).

Beyond traditional VIV research in ocean engineering, VIV in renewable energy structures, such as wind turbine blades (Grinderslev et al., 2022) and towers (Livanos, 2018), has attracted increasing attention. Computational fluid dynamics (CFD) is a currently achievable approach for investigating the VIV characteristics of prototype wind turbine blades. Researchers at the Technical University of Denmark (DTU) first achieved three-dimensional (3D) prototype blade VIV simulations with fully developed vibration regions using a coupled framework between the structural solver HAWC2 and the CFD solver EllipSys3D (Heinz et al., 2016). Horcas et al. (2020) extended this framework to the International Energy Agency (IEA) 10-MW reference blade (Bortolotti et al., 2019), systematically investigating the VIV response under various combinations of inclination and pitch angles at a fixed inflow velocity of $18\,\mathrm{m/s}$. They found that tip geometry can significantly influence VIV behavior and completely suppress VIV with a few degrees of variation.

Subsequent work by Horcas et al. (2022b) greatly expanded the parametric space by performing 448 high-fidelity fluid-structure interaction simulations covering inclination angles from $0°$ to $70°$ and pitch angles from $70°$ to $110°$. This comprehensive mapping revealed distinct excitation mechanisms at high and low inclination angles and highlighted both similarities and differences with classical two-dimensional VIV. In parallel, Horcas et al. (2022a) examined the potential of static trailing-edge flaps for VIV mitigation on the same blade, showing that while certain deflection angles reduce vibration amplitudes, the mitigation effect is generally limited and primarily shifts the VIV risk to other inflow conditions.

In addition to the fully coupled fluid-structure interaction studies, Grinderslev et al. (2022) introduced the forced motion method as a computationally efficient alternative for blade VIV analysis. By prescribing structural mode shapes and amplitudes, forced motion simulations are able to predict the VIV amplitude based on the balance of aerodynamic power and structural dissipation power. This method is similar to the riser VIV prediction framework in ocean engineering (Zhao et al., 2024). Grinderslev et al. (2023) systematically evaluated the influence of grid resolution, turbulence modeling, and a CFD solver on three-dimensional blade VIV predictions, showing that cases with low inclination angles require finer meshes and higher-fidelity turbulence models; extensive considerations are needed when modeling 3D VIV using CFD.

As noted above, most previous studies have focused on tip displacement rather than the full structural response of the blade, and few have been openly accessible. In this paper, we present the National Laboratory of the Rockies' (NLR's) work to simulate three-dimensional VIV of the prototype IEA 10-MW wind turbine blade using the open-source ExaWind framework at realistic Reynolds numbers. The study first investigates the effects of (1) blade mesh resolution, (2) time step size, and (3) VIV triggering methods to establish an optimal setup for blade VIV simulations. Then, using the setup, the VIV response characteristics of the IEA 10-MW blade, including amplitude, frequency, and phase distributions along the span, are analyzed and compared with published DTU results for cross-validation. In addition, the influence of reduced velocity is preliminarily examined and compared with conventional flexible pipe VIV behavior.

The paper is organized as follows. Section 2 describes the simulation methodology, including the ExaWind framework, CFD mesh generation, and simulation setup. Section 3 presents the modal analysis approach for the wind turbine blade and validates the mode shapes of the IEA 10-MW blade against results reported by DTU. Section 4 discusses the sensitivity study results for VIV simulations, examining the effects of mesh resolution, time step size, and VIV triggering method. Section 5 presents the modal analysis results and primary VIV response characteristics in detail. Finally, Section 6 summarizes the key findings and conclusions of this study.

2. Simulation methodology

This section presents the numerical methodology employed in the present study. An overview of the ExaWind computational framework is provided, followed by detailed descriptions of its components employed in this work: Nalu-Wind, AMR-Wind, OpenFAST, and TIOGA. Then, the mesh generation for the blade (near-body) and background (off-body) domains are described. Finally, the differences in simulation setup between the present study and that of DTU are outlined.

2.1. ExaWind stack

The ExaWind stack (Sprague et al., 2020; Sharma et al., 2024) is an open-source suite of computational physics codes developed to simulate key flow phenomena in wind energy applications, spanning airfoils, individual wind turbines, and entire wind farms. The stack consists of multiple codes for CFD, structural dynamics, and a coupling framework that wraps all the codes and enables multi-physics simulations. The ExaWind stack is designed for execution on modern high-performance computing architectures, supporting both conventional central processing units (CPUs) and graphics processing units from multiple vendors. In this study, the unstructured-grid flow solver Nalu-Wind was used to resolve the blade mesh, while the block-structured adaptive mesh flow solver AMR-Wind

Table 1
Mesh settings used for sensitivity study. Nalu-Wind mesh is the near-body mesh setting, and AMR-Wind mesh is the background mesh setting.

Index	Nalu-Wind Mesh (chordwise × spanwise nodes)	AMR-Wind Mesh
1	C385S317: 385 × 317 with approximate 14 million cells	three layers ≈ 67.5 million cells
2	C385S662: 385 × 662 with approximate 27 million cells	
3	C385S1001: 385 × 1001 with approximate 40 million cells	
4	C513S317: 513 × 317 with approximate 19 million cells	
5	C513S662: 513 × 662 with approximate 37 million cells	

was applied for off-body CFD simulations. The TIOGA library served as the overset grid assembler between the two flow solvers, and OpenFAST was employed for structural dynamics analysis coupled with Nalu-Wind.

Nalu-Wind (Sharma et al., 2024) is an incompressible-flow, unstructured-grid, finite-volume CFD solver. The code supports a wide range of turbulence modeling approaches, from Reynolds-averaged Navier-Stokes to large-eddy simulations. Temporal discretization is performed using the second-order backward differentiation formula, resulting in a coupled system of nonlinear equations that must be solved iteratively at each time step. This system is solved using a Picard iteration in conjunction with a linear pressure-Poisson equation. The resulting linear systems are handled by Krylov subspace solvers and preconditioners through the hypre libraries (Falgout and Yang, 2002). In the present work, four Picard iterations were used, ensuring a reduction of the nonlinear residual for the momentum equations by approximately 2.4 orders of magnitude. For turbulence modeling, we employ the Improved Delayed Detached Eddy Simulation (IDDES) model (Gritskevich et al., 2012). The IDDES implementation in ExaWind has been validated for three-dimensional airfoils over angles of attack ranging from 0° to 90° (Bidadi et al., 2023) and for a horizontal-axis wind turbine (Bidadi et al., 2025).

AMR-Wind (Kuhn et al., 2025) is an incompressible flow, block-structured grid, finite-volume flow solver built on the AMReX library (Zhang et al., 2019). It supports large-scale parallel computing and both static and dynamic mesh refinement. The solver includes turbulence models ranging from Reynolds-averaged Navier-Stokes to large-eddy simulations and can run independently for atmospheric boundary layer and wind farm simulations using actuator disk or actuator line methods. In this study, AMR-Wind was used for off-body simulations with the same turbulence model (IDDES) as Nalu-Wind. Due to the highly complex and massively separated flows from the blade, the static mesh refinement was employed with mesh refinement zones defined prior to the simulations to avoid any issues or complexities caused by dynamic mesh refinement. Details about the mesh refinement will be presented in the mesh generation section.

OpenFAST (Jonkman et al., 2025) is an open-source tool for simulations of wind turbines. OpenFAST integrates low- and mid-fidelity engineering models, including aerodynamics, hydrodynamics, structural dynamics, environmental loading, control, and power generation. Within the ExaWind framework, OpenFAST can be coupled with high-fidelity CFD solvers, Nalu-Wind, and AMR-Wind. In this study, OpenFAST was coupled with Nalu-Wind to perform blade-resolved fluid-structure interaction simulations. The blade's structural dynamics were computed using the BeamDyn module of OpenFAST, which is based on geometrically exact beam theory. At each time step, aerodynamic loads from Nalu-Wind were transferred to OpenFAST, and the resulting blade deformations were fed back to Nalu-Wind and applied to the blade mesh. The details about coupling between Nalu-Wind and OpenFAST can be found in Sprague et al. (2020).

2.2. Mesh generation

The blade mesh for Nalu-Wind was generated based on the YAML ontology of the IEA 10-MW reference turbine available in the GitHub repository (Bortolotti et al., 2019). The pressure and suction sides of the blade surface were first created in Plot3D format, with the number of points in the chordwise and spanwise directions specified by the user. For spanwise resolution, the number of points was defined as points per unit chord length at selected radial positions. The volume mesh was then generated using pyHyp, a hyperbolic mesh generator (Secco et al., 2021), with user-defined inputs for initial wall-normal spacing, the number of wall-normal grid points, and the outer-boundary extent. The resulting multi-block structured mesh was converted into the Exodus II format for use in Nalu-Wind.

The AMR-Wind (off-body) computational domain was generated using its built-in domain generation capability. The domain extends from $-512\,\mathrm{m}$ to $512\,\mathrm{m}$ in all X, Y, and Z directions. Two levels of static mesh refinement were applied within the region spanning $-170\,\mathrm{m}$ to $170\,\mathrm{m}$ in all directions. The base grid spacing is $4\,\mathrm{m}$, and the finest grid spacing is $1\,\mathrm{m}$, resulting in a total of about 67.5 million cells in the AMR-Wind domain.

Five Nalu-Wind meshes with different grid resolutions (two chordwise and three spanwise resolutions) were generated for a grid-sensitivity study, as Table 1 shows. C385S317 denotes a grid with 385 chordwise mesh nodes and 317 spanwise nodes, with approximately 14 million cells in total; C385S662 denotes a grid with 385 chordwise mesh nodes and 662 spanwise nodes, with approximately 27 million cells in total; C385S1001 denotes a grid with 385 chordwise mesh nodes and 1001 spanwise nodes, with approximately 40 million cells in total; C513S317 denotes a grid with 513 chordwise mesh nodes and 317 spanwise nodes, with approximately 19 million cells in total; and C513S662 denotes a grid with 513 chordwise mesh nodes and 662 spanwise nodes, with approximately 37 million nodes in total. All meshes satisfy $y^+ < 1$. The AMR-Wind background mesh is kept constant with $512\,\mathrm{m} \times 512\,\mathrm{m} \times 512\,\mathrm{m}$ domain size. All blade meshes employed the same initial wall-normal spacing of 5×10^{-6} m, 99 grid points in the wall-normal direction, and an outer-boundary size of $35\,\mathrm{m}$, resulting in a wall-normal growth rate of 1.15.

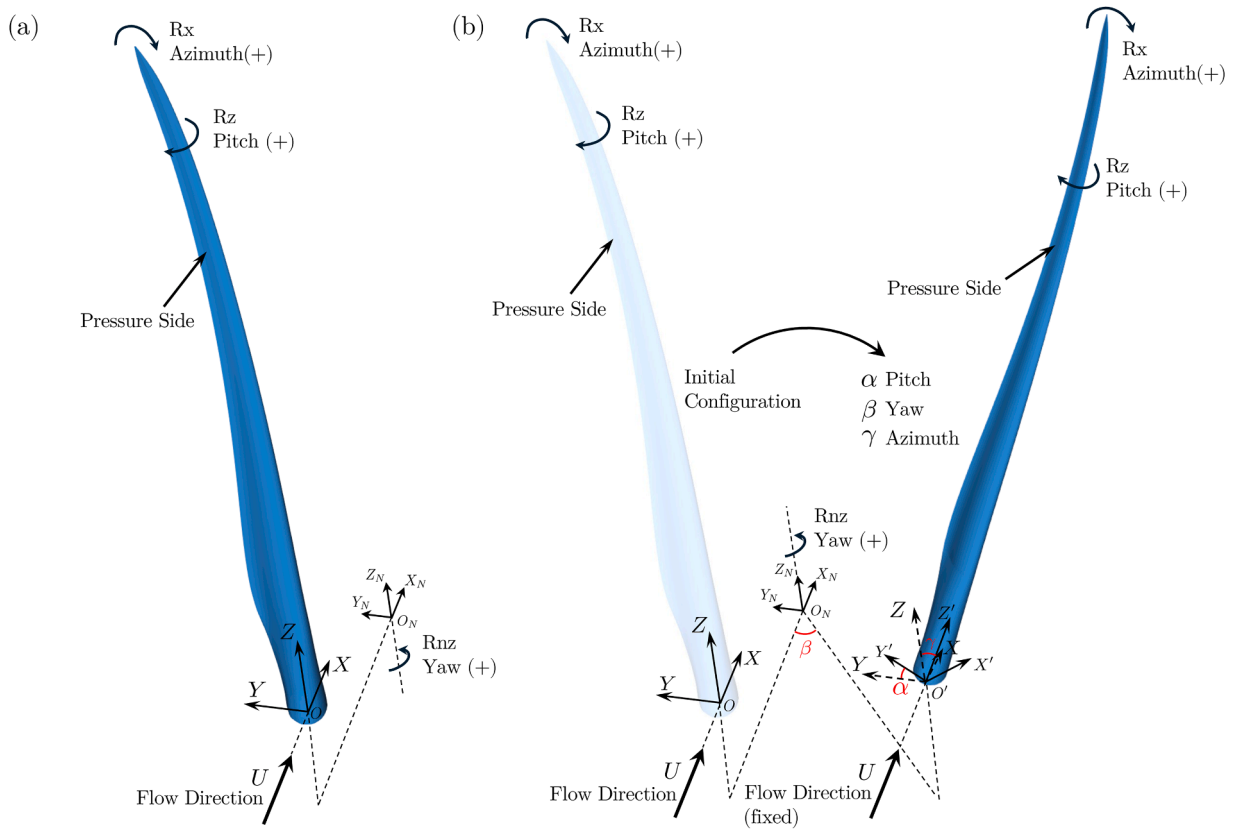

Fig. 1. Coordinate definition for the blade VIV system: (a) Initial configuration. O denotes the geometric center of the blade root section, and O-XYZ represents the initial OpenFAST blade coordinate system (Jonkman et al., 2025). O_N-$X_N Y_N Z_N$ corresponds to the nacelle coordinate system, which remains fixed in the present study. The inflow direction is aligned with the positive X-axis toward the pressure side of blade, with uniform distribution with U. Yaw (Y) is defined as the rotation of the Z_N-axis following the right-hand rule, pitch (P) is defined as the rotation of the Z-axis following the left-hand rule, and azimuth rotation (A) is defined as the rotation of the X-axis following the right-hand rule. (b) Configuration after rotations. Sequence of operations is defined as follows: α degrees for pitch, β degrees for yaw, and γ degrees for azimuth rotation. The flow direction keeps unchanged after operation and the angles are illustrated in the figure.

The OpenFAST coordinate system for the blade model is shown in Fig. 1 and used in the present study; the total length of the blade is about 97.325 m. In the present study, the inflow direction is fixed, and the motion comprises yaw, pitch, and azimuth rotation. The computational domain in the present study is shown in Fig. 2.

2.3. Simulation setup comparison with DTU stack

Grinderslev et al. (2022, 2023) from DTU performed a simulation of the IEA 10-MW blade based on the HAWC2 and EllipSys3D coupled framework. There are a few differences between DTU's and NLR's implementations. To avoid confusion for future researchers, we outline these differences below:

1. Motion sequence in the present study: pitch → azimuth rotation → yaw.
2. Pitch angle α in NLR convention is 180° minus pitch angle in DTU convention.
3. Azimuth rotation angle γ in NLR convention is 360° minus inclination angle in DTU convention.
4. In the present work, the inflow direction was fixed while the blade position was adjusted, as shown in Fig. 1, whereas in the DTU study, the blade was fixed and the inflow direction was varied.
5. There is a slight geometrical difference in the near-tip region of the IEA 10-MW blade. Fig. 3 shows the detailed structure difference; the NLR IEA 10-MW refers to the model used for OpenFAST simulations, and the DTU IEA 10-MW refers to the model used for HAWC2 simulations. The tip chord length of NLR model is smaller than that of DTU model, which is about 0.5 m [personal communication with Prof. Niels Nørmark Sørensen, April 2025]. As shown later, VIV occurs primarily near the tip. We do not analyze the influence of this tip geometry difference here. It will be addressed in future work.

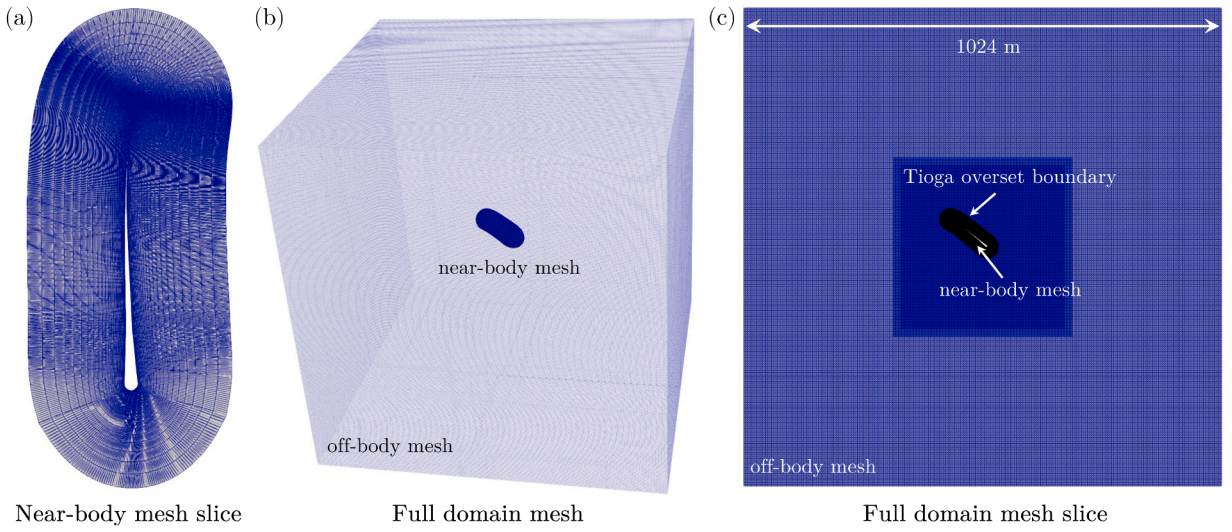

Fig. 2. Computational domain in the present study with C385S662 mesh and P80A310 case: (a) Near-body mesh slice in Nalu-Wind. (b) Full computational domain including off-body mesh in AMR-Wind and near-body mesh in Nalu-Wind. (c) Full domain mesh slice.

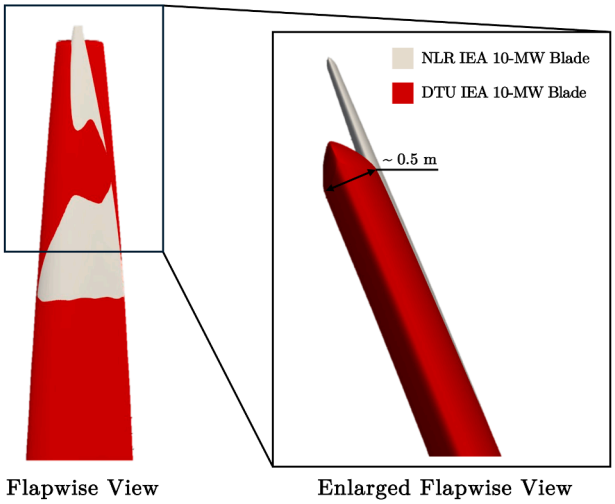

Fig. 3. Comparison of near-tip geometry between NLR IEA 10-MW blade (geometry for OpenFAST) and DTU IEA 10-MW blade (geometry for HAWC2). Gray: NLR IEA 10-MW blade. Red: DTU IEA 10-MW blade.

3. VIV Analysis methodology

In this section, we first introduce the modal analysis methodology for the wind turbine blade, including both undamped and complex modal analyses. We then cross-validate the mode shapes obtained in this study against the published results from the DTU stack (Horcas et al., 2022a).

3.1. Modal analysis of a wind turbine blade

3.1.1. Undamped modal analysis of wind turbine blade

The governing equation for a single blade in BeamDyn (Wang et al., 2016) after linearization (Jonkman et al., 2018) can be treated as:

$$[M]\{\ddot{\xi}(t)\} + [C]\{\dot{\xi}(t)\} + [K]\{\xi(t)\} = \{f(t)\} \tag{1}$$

where $[M]$, $[C]$ and $[K] \in \mathbb{R}^{N\times N}$ are the mass, damping, and stiffness matrices, respectively. $N = 6N_{node}$ is the number of structural degrees of freedom (DOFs), and N_{node} is the number of nodes. $\{\xi(t)\}$, $\{\dot{\xi}(t)\}$, $\{\ddot{\xi}(t)\}$ and $\{f(t)\} \in \mathbb{R}^{N\times 1}$ are displacement, velocity, acceleration, and external force vectors at time t, respectively. The structural properties of the IEA-10MW wind-turbine blade are

taken from Bortolotti et al. (2019). In the OpenFAST model, a stiffness-proportional damping model is adopted, with 6-DOF damping ratios of $[2.55\times10^{-3},\ 1.53\times10^{-3},\ 3.3\times10^{-4},\ 1.53\times10^{-3},\ 2.55\times10^{-3},\ 3.3\times10^{-4}]$.

The undamped mode can be calculated by eigenvalue analysis of $[K]$ and $[M]$ as:

$$[K][\Phi]=[M][\Phi][\Omega]^2,\quad [\Omega]=\mathrm{diag}(\omega_1,\dots,\omega_N), \tag{2}$$

where $[\Omega]$ is the eigenvalue matrix with ω_i as the angular undamped natural frequency, and $[\Phi]$ is the undamped eigenvector matrix with N-by-N size. The motion can be expressed as:

$$\{\xi\}=\sum_i \left[\Phi_i\right]\left\{q_i(t)\right\}. \tag{3}$$

Substituting Eq. (3) into Eq. (1) and multiplying by the modal shape matrix $[\Phi]^\top$, the governing equation can be expressed in modal space as:

$$m_{r,i}\ddot{q}_{r,i}(t)+c_{r,i}\dot{q}_{r,i}(t)+k_{r,i}q_{r,i}(t)=F_i(t)\quad (i=1,2,\cdots,N), \tag{4}$$

where $m_{r,i}$, $c_{r,i}$, $k_{r,i}$, and F_i are modal mass, modal damping, modal stiffness, and modal force of the ith mode, respectively. Based on the undamped modal shape, the modal weight vector can be expressed as:

$$\{q(t)\}=\left([\Phi]^\top[\Phi]\right)^{-1}[\Phi]^\top\{\xi(t)\}. \tag{5}$$

3.1.2. Complex modal analysis

In the BeamDyn module of OpenFAST, the complex modal analysis is applied. Eq. (1) can also be expressed in the state space, omitting the time argument hereafter, as:

$$\{\dot{\Xi}\}=[A]\{\Xi\}+[B]\{f\}, \tag{6}$$

where

$$\{\Xi\}=\begin{Bmatrix}\{\xi(t)\}\\ \{\dot{\xi}(t)\}\end{Bmatrix}\in\mathbb{R}^{2N\times1},\quad \{\dot{\Xi}\}=\begin{Bmatrix}\{\dot{\xi}(t)\}\\ \{\ddot{\xi}(t)\}\end{Bmatrix}\in\mathbb{R}^{2N\times1},$$

$$[A]=\begin{bmatrix}\mathbf{0}_{[N\times N]} & \boldsymbol{I}_N\\ -[M]^{-1}[K] & -[M]^{-1}[C]\end{bmatrix}\in\mathbb{R}^{2N\times2N},\quad [B]=\begin{bmatrix}\mathbf{0}_{[N\times N]}\\ [M]^{-1}\end{bmatrix}\in\mathbb{R}^{2N\times N},$$

where $\mathbf{0}$ denotes the zero matrix, $\boldsymbol{I}$ denotes the identity matrix, $\{\Xi\}$ is the state vector, $\{\dot{\Xi}\}$ is the state vector derivative, $[A]$ is the state matrix, and $[B]$ is the input matrix.

In OpenFAST, the linearization method is applied to estimate the state space matrix $[A]$ (Jonkman et al., 2018). The complex modal shape can be obtained based on matrix $[A]$; the eigenvalues matrix of $[\Lambda]\in\mathbb{C}^{2N\times2N}$ is:

$$[\Lambda]=\begin{bmatrix}\lambda_1 & & & & & & \\ & \ddots & & & 0 & & \\ & & \lambda_N & & & & \\ & & & \lambda_1^* & & & \\ & 0 & & & \ddots & & \\ & & & & & & \lambda_N^*\end{bmatrix}=\begin{bmatrix}\sigma_1+j\omega_1' & & & & & & \\ & \ddots & & & 0 & & \\ & & \sigma_N+j\omega_N' & & & & \\ & & & \sigma_1-j\omega_1' & & & \\ & 0 & & & \ddots & & \\ & & & & & & \sigma_N-j\omega_N'\end{bmatrix}, \tag{7}$$

where $(-)^*$ represents conjugate value, the real part of ith-order complex eigenvalues λ_i is $\sigma_i=-\zeta\omega_i$, ζ is the damping ratio, ω_i is the undamped angular natural frequency of ith order, and the imaginary part is $j\omega_i'$, where j is an imaginary unit and ω_i' is the damped natural frequency as $\sqrt{1-\zeta^2}\omega_i$. The undamped and damped natural frequencies can be obtained through complex modal analysis. The eigenvector can be expressed as:

$$\begin{aligned}[\Psi'] &=\begin{bmatrix}\Psi_1' & \Psi_2' & \cdots & \Psi_N' & \Psi_1'^* & \Psi_2'^* & \cdots & \Psi_N'^*\end{bmatrix}\\ &=\begin{bmatrix}\Psi & \Psi^*\\ \Psi\Lambda & \Psi^*\Lambda^*\end{bmatrix},\end{aligned} \tag{8}$$

where Ψ is a complex matrix with value of $\eta_{i,z}e^{\gamma_{i,z}j}$, z represents the spanwise location, η is the amplitude, and γ is the phase angle. It should be noted that the original rotational displacement is described in the Wiener–Milenković rotational parameters (Bauchau, 2011). Given the Wiener–Milenković parameter vector

$$\boldsymbol{w}=\begin{bmatrix}w_x, & w_y, & w_z\end{bmatrix},\qquad w=\|\boldsymbol{w}\|, \tag{9}$$

the associated rotation angle ϕ is defined as

$$\phi=4\arctan\left(\frac{w}{4}\right), \tag{10}$$

and the rotational displacement vector θ in Cartesian coordinate is expressed as

$$\theta=\phi\,\mathbf{n}=\frac{4\arctan\left(\frac{w}{4}\right)}{w}\boldsymbol{w}, \tag{11}$$

where $\mathbf{n}$ is a unit vector.

Table 2
Comparison of the natural frequencies of the first six modes. Undamped frequencies are calculated from the undamped modal analysis from Eq. (2). Damped frequencies are calculated based on the complex modal analysis from the imaginary part of Eq. (7), and the results from Horcas et al. (2022a) are adopted for comparison.

Order	Description	Undamped Frequency	Damped Frequency	Horcas et al. (2022a)
1	First Flapwise Mode	$f_{n1} = 0.4080$ Hz	0.4084 Hz	0.41 Hz
2	First Edgewise Mode	$f_{n2} = 0.6739$ Hz	0.6739 Hz	0.67 Hz
3	Second Flapwise Mode	$f_{n3} = 1.0697$ Hz	1.0696 Hz	1.07 Hz
4	Second Edgewise Mode	$f_{n4} = 1.7877$ Hz	1.7876 Hz	1.78 Hz
5	Third Flapwise Mode	$f_{n5} = 2.2718$ Hz	2.2714 Hz	2.27 Hz
6	First Edgewise & Torsion Mode	$f_{n6} = 3.7205$ Hz	3.7212 Hz	3.71 Hz

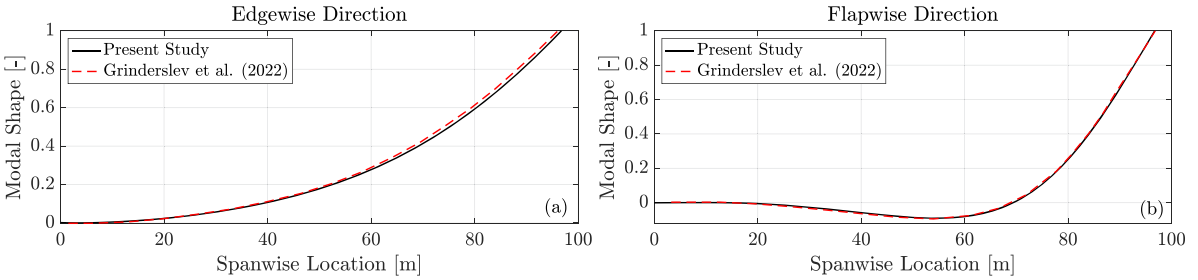

Fig. 4. The comparison of the first edgewise modal shape of IEA 10-MW turbine blade: (a) edgewise direction component and (b) flapwise direction component. Black line: result of present study. Red dashed line: result in Grinderslev et al. (2022).

Table 3
Blade configurations used for sensitivity study. α, β, and γ are the pitch, yaw, and azimuth rotation angles, respectively, as defined in Fig. 1.

Index	Configuration	Definition
1	P80A310	$\alpha = 80°$, $\beta = 90°$, $\gamma = 310°$
2	P95A310	$\alpha = 95°$, $\beta = 90°$, $\gamma = 310°$
3	P90A310	$\alpha = 90°$, $\beta = 90°$, $\gamma = 310°$
4	P95A320	$\alpha = 95°$, $\beta = 90°$, $\gamma = 320°$

3.2. Modal shape validation

Modal analysis contains two main components: mode shape and natural frequency. We compare our results with the DTU results obtained using HAWC2 (Grinderslev et al., 2022; Horcas et al., 2022a). Note that OpenFAST and HAWC2 use different versions of the IEA 10-MW model with slight differences in structural properties shown in Fig. 3. In the present study, 73 quadrature nodes are applied for the BeamDyn model, with stiffness proportional damping defined in Bortolotti et al. (2019).

Table 2 presents the comparison of natural frequencies. The natural frequencies of the first six modes are displayed and compared with the HAWC2 results reported by Horcas et al. (2022a). Mode descriptions follow Fig. 1: flapwise, bending motion primarily along the X-axis; edgewise, bending motion primarily along the Y-axis; and torsion, rotation about the Z-axis. Undamped natural frequencies are obtained from the undamped modal analysis in Eq. (2). Damped frequencies are calculated based on the complex modal analysis from the imaginary part of Eq. (7). The undamped and damped natural frequencies of the first six modes differ only slightly because of the relatively low damping ratio, and the discrepancy increases with mode number. However, this has little influence on the blade VIV, which, as shown later, is primarily dominated by the second mode. The natural frequency results match well with the DTU result from Horcas et al. (2022a).

Fig. 4 compares the mode shapes from this study with those reported by Grinderslev et al. (2022). The mode shapes are obtained from the undamped eigenvector matrix $[\Phi]$ and are nondimensionalized. The second mode (the first edgewise mode) is shown with its edgewise (Y-axis) and flapwise (X-axis) components. The modal shapes are consistent with the total length difference of the two versions of the IEA 10-MW blade structure in Fig. 4(a). The maximum spanwise coordinate reported in Grinderslev et al. (2022) is 96.089 m, whereas that in the present study is 96.755 m.

4. Sensitivity study

In order to determine the appropriate mesh resolution, time step size, and VIV triggering method for the simulations, a series of sensitivity studies are conducted. This section presents the results for (1) blade mesh resolution, (2) time step size, and (3) VIV triggering method. First, five different blade mesh resolutions are tested using a fixed time step size under four representative pitch conditions. To cross-validate the simulations against the DTU results, these conditions are selected from Horcas et al. (2022b). Next, the effect of time step size is examined using three different values for a selected mesh resolution and two representative pitch conditions identified from the mesh sensitivity study. Finally, five VIV triggering methods are evaluated, and their effects on blade tip displacement are analyzed under fixed mesh and time step conditions.

4.1. Blade mesh resolution

A sensitivity study on blade mesh resolution was conducted under four representative flow conditions from Horcas et al. (2022b): two exhibiting strong VIV and two showing limited VIV. Table 3 lists the test conditions. All the cases have a yaw angle (β) of 90° and an inflow velocity (U) of 18 m/s.

The meshes are generated based on the methodology stated in Section 2.2. The maximum mesh cell count is approximately 108 million, and the time step for mesh convergence tests is chosen as $\Delta t = 0.0025$ s, which is selected with reference to the published value of 0.006 s (Horcas et al., 2020). Fig. 5 shows the mesh convergence test results with four different configurations and mesh settings; subfigures (a) to (d) present the maximum translational response of the tip node, and subfigures (e) to (h) present the maximum rotational response of the tip node. As an example, the maximum flapwise translation and rotation responses about the X-axis are computed from root-mean-square (RMS) values as:

$$A_{x,max} = \sqrt{2}\,\xi_{xt,rms}, \qquad \theta_{x,max} = \sqrt{2}\,\xi_{rxt,rms}, \tag{12}$$

where $\xi_{xt,rms}$ and $\xi_{rxt,rms}$ are the RMS values of the corresponding demeaned components over the steady VIV period window at the tip node, which isolates the fluctuating VIV response. The components of the other DOFs are computed in a similar way. The results indicate that two of the four configurations, P80A310 and P95A310, exhibit significant VIV, with $A_{y,max}$ above 1.00 m, as shown in Fig. 5(a) and (c). On the other hand, P90A310 and P95A320 show only limited vibration, with $A_{y,max}$ about 0.02 m, as shown in Fig. 5(b) and (d). Edgewise vibration dominates the response. The average chord length of the IEA 10-MW blade is $\bar{c} = 3.72$ m. The maximum vibration amplitudes correspond to nondimensional values of approximately $0.27\bar{c}$ for the strongly responding cases and less than $0.01\bar{c}$ for the weakly responding cases. Among the rotational DOFs, only rotation about the Z-axis (torsion) exhibits a comparatively large response of about 2.0°, shown in Fig. 5(e) and (g). The remaining two configurations likewise show only limited rotational motion, on the order of $\mathcal{O}(10^{-3})$ degrees, as shown in Fig. 5(f) and (h). Consistent with Horcas et al. (2020), we observe the same pattern: two cases (P80A310, P95A310) exhibit significant VIV, whereas the other two (P90A310, P95A320) display limited vibration. Meanwhile, as shown in Fig. 5(a) and (c), spanwise resolution plays an important role in the convergence of the vibration response. Consistent with this observation, our previous IDDES simulations also demonstrated strong sensitivity to spanwise resolution under deep-stall conditions for three-dimensional airfoils (Bidadi et al., 2023) where pronounced flow separation is also observed.

Table 4 shows the selected peak vibration amplitudes, $A_{x,max}$, $A_{y,max}$, and $\theta_{z,max}$, for the two configurations (P80A310 and P95A310), exhibiting pronounced VIV across five meshes (C385S317, C385S662, C385S1001, C513S317, and C513S662). The maximum responses for both configurations exhibit limited sensitivity to mesh resolution, with translational variations across the five meshes within approximately 5% to 10% and in close agreement with Horcas et al. (2022b). Among the mesh settings, C385S662 provides the most consistent match to the reference values. For P80A310, it yields $A_{x,max} = 0.20$ m, $A_{y,max} = 1.19$ m, essentially coincident with the literature (Horcas et al., 2022b). For P95A310, it gives $A_{x,max} = 0.21$ m, $A_{y,max} = 1.23$ m, all within about 5% of the published benchmarks. It should be noted that the rotational DOFs differ between the datasets: the published results report about 0.5°, whereas the ExaWind results are about 2°, but this rotational response remains small. The discrepancy is likely attributable to slight differences between the OpenFAST and HAWC2 IEA 10-MW blade models. Considering fidelity to the reference data alongside computational cost, C385S662 is selected as the mesh setting for further analysis.

4.2. Time step size

The time step convergence tests are conducted based on the C385S662 mesh setting. Fig. 6 shows the time step convergence results for three time steps, $\Delta t = 0.005$ s, 0.0025 s, and 0.001 s, and the corresponding nondimensional time steps $U\Delta t/\bar{c}$ are 0.0242, 0.0121, and 0.0048, respectively. For the mesh convergence studies we adopted $\Delta t = 0.0025$ s, whereas the published work used 0.006 s (Horcas et al., 2022b). As an example, in the two configurations with obvious VIV, P80A310 and P95A310, the peak transverse amplitudes $A_{y,max}$ across the three time steps $\Delta t \in \{0.005\,\text{s}, 0.0025\,\text{s}, 0.001\,\text{s}\}$ are 0.99 m, 1.19 m, and 1.29 m for P80A310, and 1.40 m, 1.23 m, and 1.22 m for P95A310. The responses obtained with the three time steps are very similar; in particular, the responses for $\Delta t = 0.0025$ s and 0.001 s are nearly the same, indicating time step independence over this range. The time step of 0.0025 s is selected as the final setup.

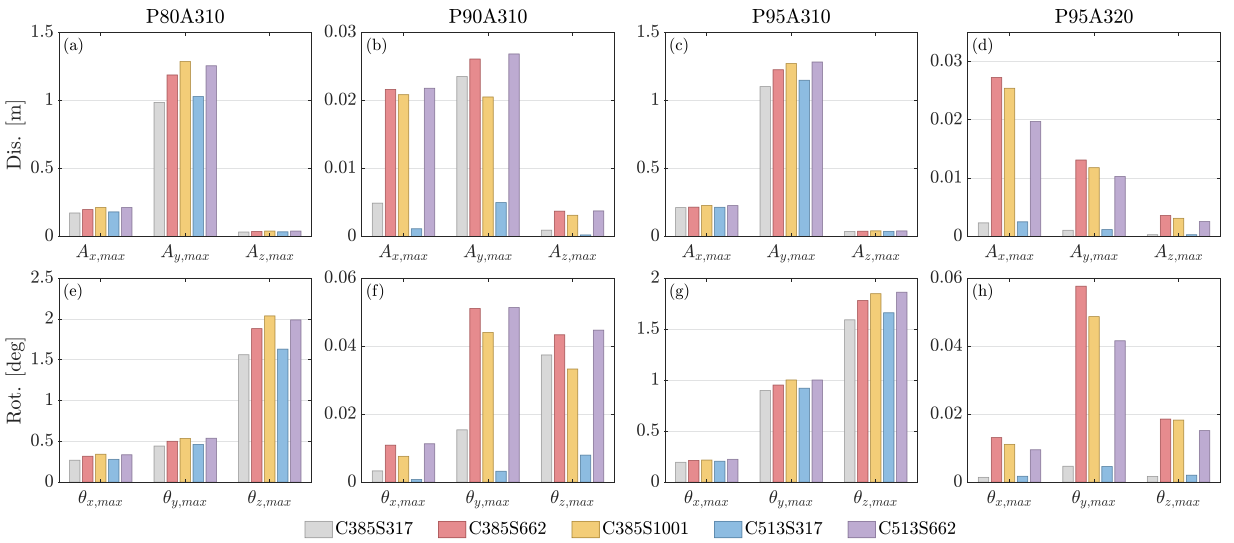

Fig. 5. Mesh convergence test result. (a)–(d) Maximum translational response. (e)–(h) Maximum rotational response. Four configurations are shown in each column: P80A310, P90A310, P95A310, and P95A320. Five kinds of mesh are shown in each subfigure: C385S317 , C385S662 , C385S1001 , C513S317 , and C513S662 .

Table 4
Selected maximum vibration amplitudes, $A_{x,max}$, $A_{y,max}$, and $\theta_{z,max}$, for the two configurations exhibiting pronounced VIV across five meshes, compared with published results in Horcas et al. (2022b).

		C385S317	C385S662	C358S1001	C513S317	C513S662	Horcas et al. (2022b)
P80A310	$A_{x,max}$ [m]	0.17	0.20	0.21	0.18	0.20	≈ 0.20
	$A_{y,max}$ [m]	0.99	1.19	1.29	1.03	1.22	≈ 1.20
	$\theta_{z,max}$ [°]	1.56	1.88	2.03	1.63	1.94	≈ 0.45
P95A310	$A_{x,max}$ [m]	0.21	0.21	0.23	0.21	0.22	≈ 0.22
	$A_{y,max}$ [m]	1.10	1.23	1.27	1.15	1.28	≈ 1.19
	$\theta_{z,max}$ [°]	1.59	1.78	1.84	1.66	1.86	≈ 0.40

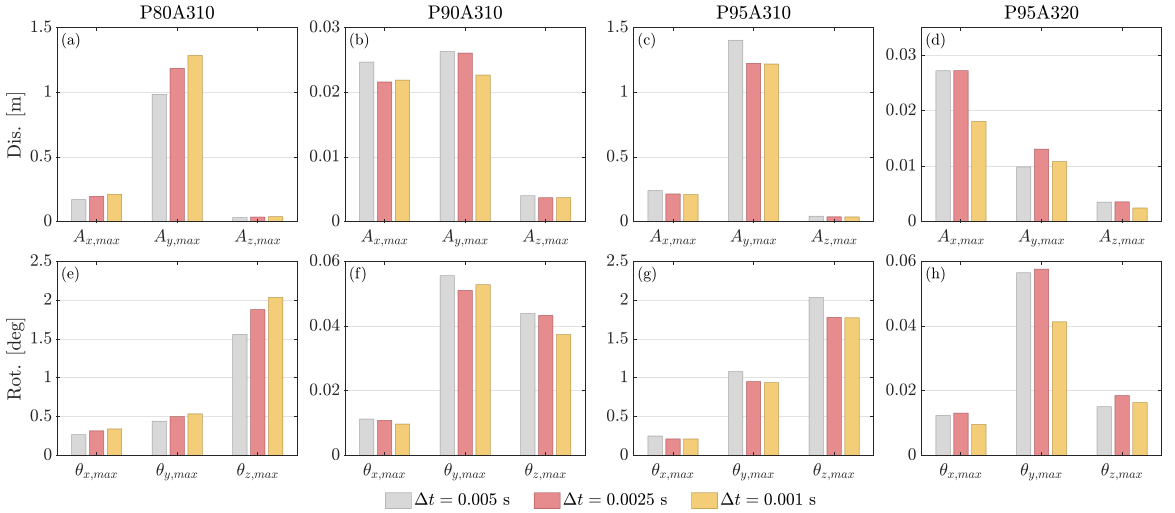

Fig. 6. Time step convergence test result. (a)–(d) Maximum translational response. (e)–(h) Maximum rotational response. Results of three different time steps are displayed: $\Delta t = 0.005$ s , $\Delta t = 0.0025$ s , and $\Delta t = 0.001$ s .

Table 5
Blade VIV triggering methods. All the force is applied in the tip node with translational force in the Y-direction..

Method	Description
1	Zero external force
2	Force ramps linearly from 0 to 2×10^3 N over 0 to 10 s , then ramps down to 0 from 10 to 11 s
3	Force with 4×10^3 N with the same ramping stage above
4	Force with 8×10^3 N with the same ramping stage above
5	Harmonic force of 4×10^3 N with frequency of 0.67 Hz with the same ramping stage above

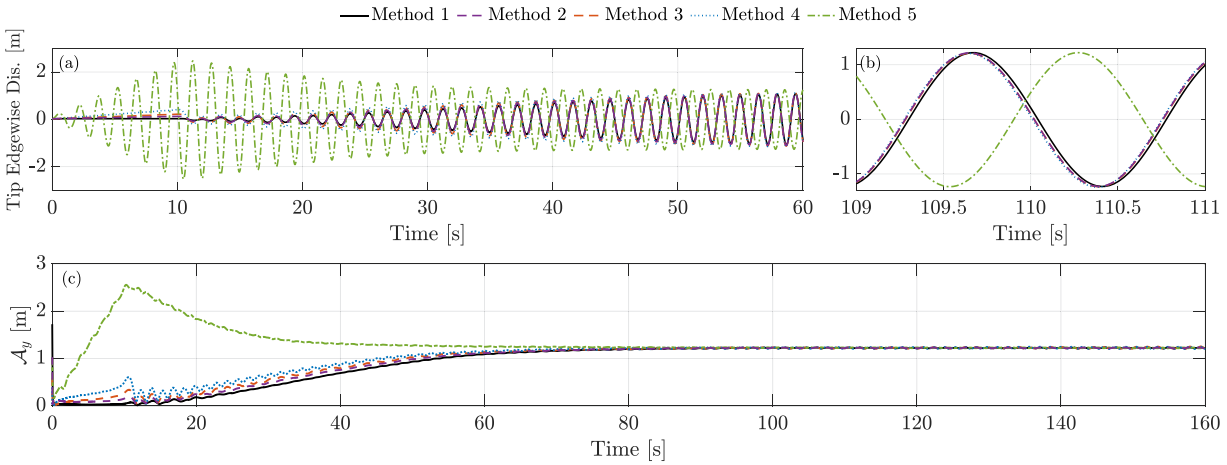

Fig. 7. Comparison of results among different VIV triggering methods in the P95A310 case: (a) Tip displacement in the edgewise direction based on different methods. (b) Fully developed edgewise tip displacement. (c) Instantaneous envelope $\mathcal{A}_y$ based on Hilbert transform. The different methods are described in Table 5. Method 1, black line –; Method 2, purple dashed line - -; Method 3, orange dashed line - -; Method 4, blue dots · · ·; Method 5, green dash-dotted line -·-. (For interpretation of the references to colour in this figure legend, the reader is referred to the web version of this article.)

4.3. VIV Triggering method

Given the high computational cost of simulations with ~108 million mesh cells, we compared five VIV triggering methods as shown in Table 5. The first method is a case with no external forcing. The second to fourth methods are ramping cases in which a prescribed force increases linearly from zero to its set value over zero to 10 s and then decreases linearly back to zero over 10–11 s, with peak magnitudes 2×10^3 N, 4×10^3 N, and 8×10^3 N. The fifth method is a harmonic force case consisting of a sinusoidal force of amplitude 4×10^3 N with frequency of 0.67 Hz, applied with a linear ramping from zero to full amplitude over 0 to 10 s and ramping down until 11 s. All the force is applied at the tip node with translational force in the Y-direction.

Fig. 7 compares VIV triggering methods for the P95A310 case. Subfigure (a) shows the tip edgewise displacement during the first 60 s; subfigure (b) presents the fully developed edgewise tip response; and subfigure(c) shows the instantaneous envelope $\mathcal{A}_y$ of the tip edgewise motion, obtained via the Hilbert transform as

$$\mathcal{A}_y(t) = \left| \xi_{yt}(t) + i\,\mathcal{H}\left[\xi_{yt}(t)\right] \right|, \tag{13}$$

where $\mathcal{H}(-)$ denotes the Hilbert transform and $\xi_{yt}(t)$ is the demeaned edgewise (Y-axis) displacement of the tip node. In Fig. 7(a), different triggering methods produce distinct VIV development: Method 2 to Method 4 exhibit a pull-release behavior, whereas Method 5 (harmonic forcing) yields a large initial harmonic response. Fig. 7(b) indicates that the fully developed VIV vibration is essentially identical across methods. Fig. 7(c) shows the instantaneous envelopes of VIV response calculated by Eq. (13), which further confirms that the instantaneous envelopes of VIV eventually converge to the same value.

Fig. 8 compares the results based on different VIV triggering methods for the P80A310 case. All approaches converge except Method 1 to essentially the same stable amplitude but on different time, as Fig. 8(a) shows. Method 1 had not converged until 250 s (requiring about 10 days of high-performance computing wall time), whereas Methods 2 and 3 reach convergence at approximately 250 s and 150 s, respectively. Methods 4 and 5 reach the convergence at approximately 100 s, as Fig. 8(b) shows. Considering the computational efficiency, Method 4 is adopted for the following simulation, and it should be noted that Method 4 is also used in the sensitivity studies, including the blade mesh resolution and time step size analyses. Meanwhile, the VIV triggering approaches adopted in the present study are specific to the IEA-10MW blade and are designed to accelerate VIV development while avoiding numerical divergence.

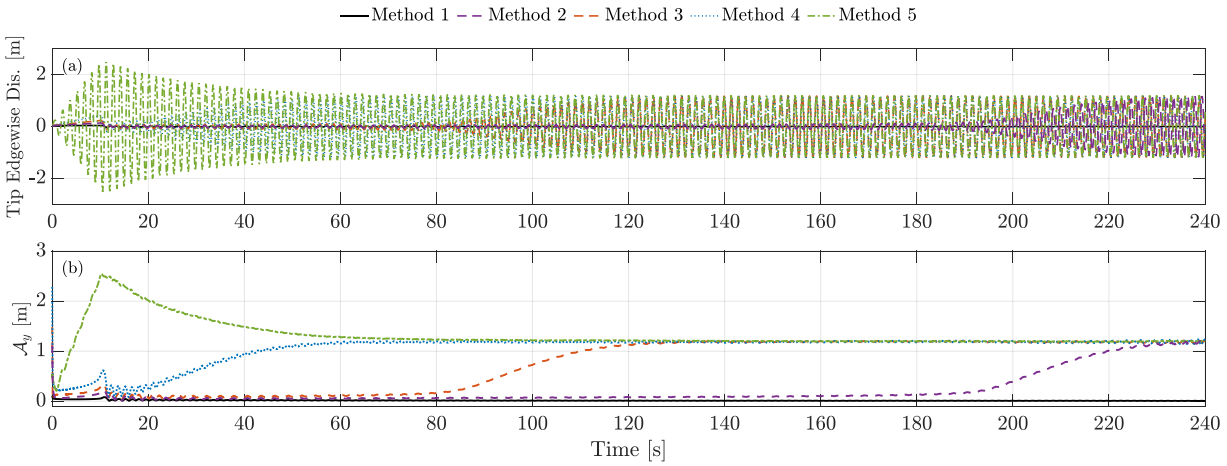

Fig. 8. Comparison of results among different VIV triggering methods in the P80A310 case: (a) Tip displacement in the edgewise direction based on different methods. (b) Instantaneous envelope $\mathcal{A}_y$ based on Hilbert transform. The different methods are described in Table 5.

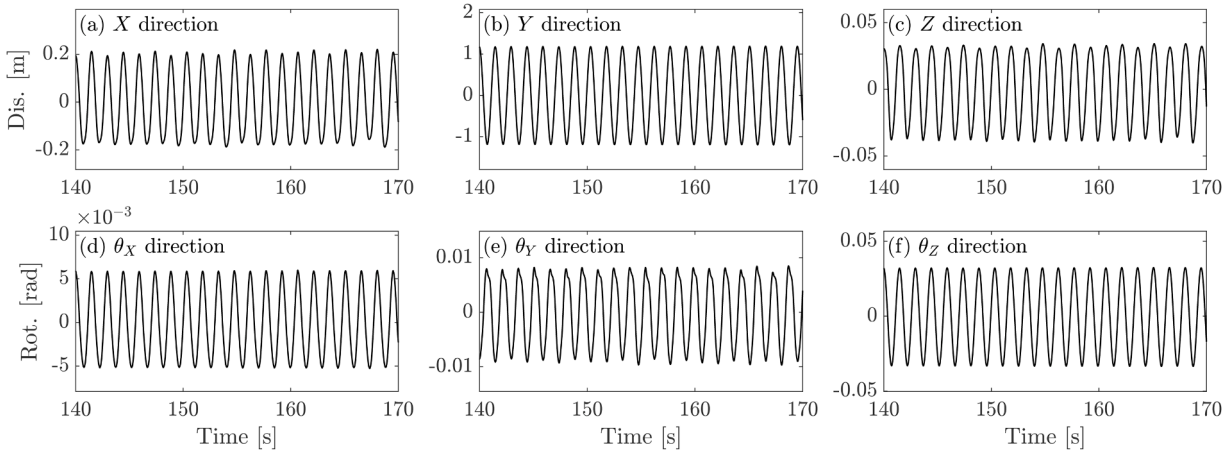

Fig. 9. Stable VIV displacement of six DOFs of P80A310 case: (a) X-direction, (b) Y-direction, (c) Z-direction, (d) θ_X-direction, (e) θ_Y-direction, and (f) θ_Z-direction.

In conclusion, for the ExaWind-based VIV simulations of a single IEA 10-MW blade in the present study, the C385S662 mesh with a time step of 0.0025 s (as shown in Table 1) is adopted, and VIV is triggered using Method 4, as shown in Table 5. The simulation is performed on NLR's Kestrel high-performance computing system; each case is run on 14 CPU nodes (1456 CPU cores) for approximately 10 days of wall-clock time.

5. Results and discussion

In this section, we present the modal analysis results for two previously identified cases, P80A310 and P95A310, that exhibit obvious vortex-induced vibration. We characterize the primary VIV characteristics, including spanwise distribution, wavelet-based time-varying response, and the traveling wave phenomenon, and finally we preliminarily examine how the VIV response varies with reduced velocity.

5.1. Modal analysis result

In this section, we perform a modal analysis of blade VIV for P80A310 and P95A310. Fig. 9 shows the stable (steady-state) VIV displacement for all six DOFs in the P80A310 case. Consistent with Fig. 5 and Fig. 6, the y (edgewise) displacement dominates the VIV response. The maximum flapwise amplitude (about 0.2 m) is about 20% of the edgewise amplitude, whereas the Z direction amplitude is less than 5%. For the rotational DOFs, rotation about θ_Z dominates, but the response remains small at less than 0.05°. Fig. 10 shows the VIV response similar with P95A310 case with significant vibration in the edgewise direction; θ_Z rotation about Z axis dominates the rotational DOFs.

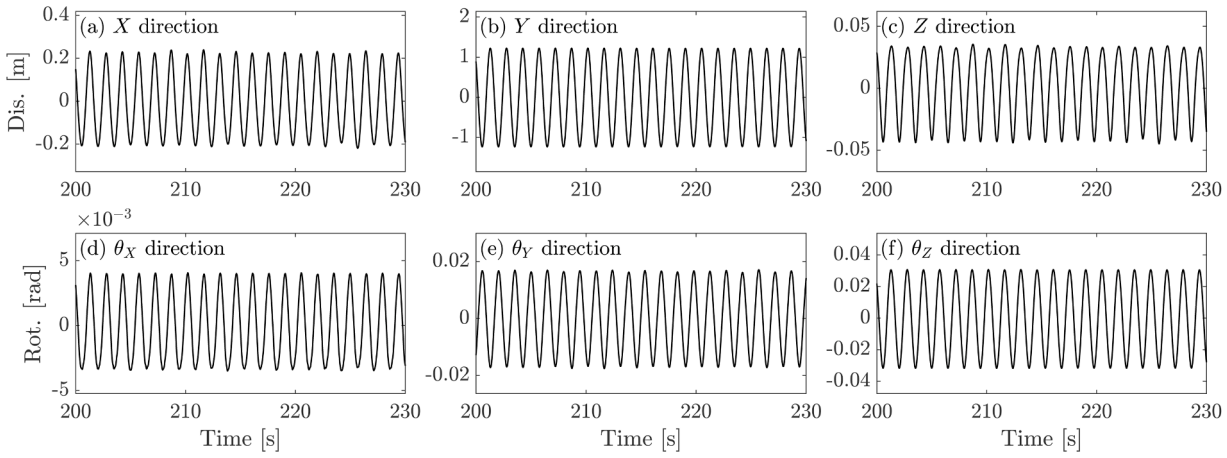

Fig. 10. Stable VIV displacement of six DOFs of P95A310 case: (a) X-direction, (b) Y-direction, (c) Z-direction, (d) θ_X-direction, (e) θ_Y-direction, and (f) θ_Z-direction.

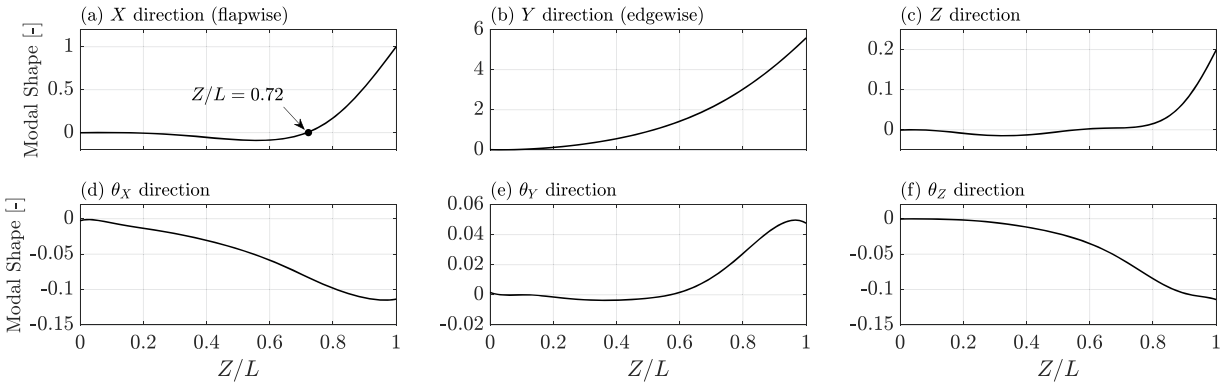

Fig. 11. Six-DOF components of the second mode. The mode shapes are normalized to unit modal mass: (a) X-direction, (b) Y-direction, (c) Z-direction, (d) θ_X-direction, (e) θ_Y-direction, and (f) θ_Z-direction.

Following Eq. (2), the mode-shape matrix $[\Phi]$ is normalized to unit modal mass, which means the modal mass m_r in Eq. (4) equals 1 for every mode. In conventional VIV studies of flexible pipes (Huera-Huarte, 2006; Fu et al., 2022a), an alternative normalization is often adopted in which each mode is scaled to unit peak amplitude. Moreover, for flexible pipes the in-line and cross-flow directions are typically analyzed as decoupled. This decoupling is generally inappropriate for wind turbine blades because of the structural complexity. The alternative normalization $[\Phi']$ is obtained by normalizing the mode shapes with respect to the edgewise direction for each mode since the edgewise response is dominant, as shown in Fig. 9 and Fig. 10. Then, two kinds of modal weight can be calculated based on Eq. (5).

The modal shape of the second mode is shown in Fig. 11; the x-axis is normalized by the blade length $L = 96.755$ m. There is an upcrossing zero location about $Z/L = 0.72$ in the modal shape in the X-direction, as shown in Fig. 11(a). Among the six DOFs, the flapwise and edgewise displacements dominate this mode. As an early-stage investigation of VIV response characteristic analysis, we primarily investigate the coupling between these two DOFs to see whether it is similar to the in-line/cross-flow coupling phenomenon in flexible pipe VIV.

Fig. 12 and Fig. 13 show the normalized modal weight of the P80A310 and P95A310 cases, respectively. The RMS values of the modal weights are normalized by the maximum value across modes, shown in the figures. The descriptions of the first five modes are shown in Table 2. The sixth to tenth modes involve more complex coupling with multi-DOF components. The figures indicate that blade VIV is dominated by the second mode, with only a minor first-mode contribution, approximately 2% of the second modal weight, shown in Fig. 13(a).

5.2. VIV Response characteristics

As noted above, the modal analysis indicates that the vibration is dominated by the second mode in both cases with limited participation from other modes. In this subsection, we conduct a preliminary investigation of VIV response characteristics considering the mode coupling.

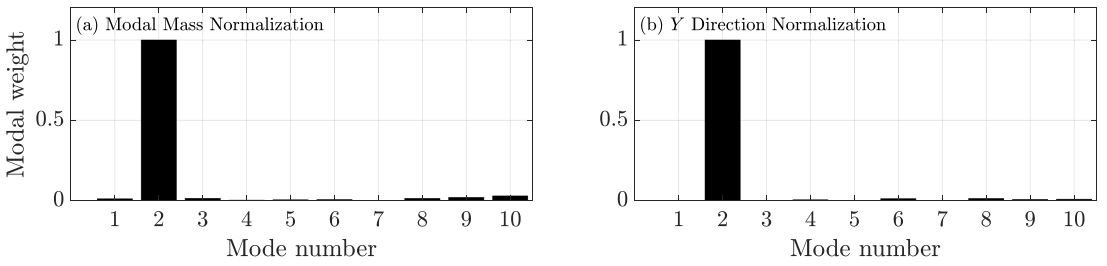

Fig. 12. Normalized modal weight of the P80A310 case: (a) modal weight based on modal mass normalization modal shape and (b) modal weight based on edgewise direction normalization modal shape.

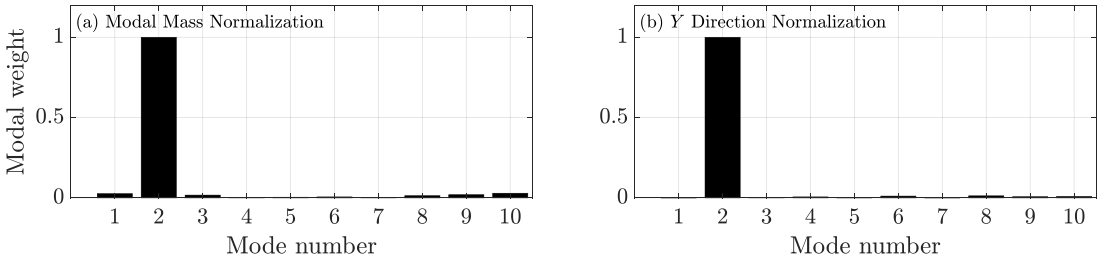

Fig. 13. Normalized modal weight of the P95A310 case: (a) modal weight based on modal mass normalization modal shape and (b) modal weight based on edgewise direction normalization modal shape.

5.2.1. P80A310 Case

Fig. 14 shows the spanwise VIV response distribution for the P80A310 case. Subfigure (a) shows the nondimensional maximum VIV displacement distribution following Eq. (12) for all nodes. Subfigure (b) shows the edgewise VIV response frequency distribution via the normalized power spectral density (PSD) of the spanwise response. The PSD results are scaled by its maximum value to unity at each node. The x-axis is nondimensionalized by the second modal natural frequency (consistent with the observed second-mode-dominated VIV), and the first, third, and fourth modal natural frequencies are marked in black dashed lines. Subfigure (c) shows the corresponding flapwise VIV response frequency distribution. Subfigure (d) shows the histogram of phase difference ϕ_{xy}, which is expressed as (Fu et al., 2022a):

$$\phi_{xy}(z,t) = \left[\phi_x(z,t) - \frac{\hat{f}_x(z,t)}{\hat{f}_y(z,t)}\phi_y(z,t), \quad \mod 360^\circ\right], \tag{14}$$

where $\phi_x(z,t)$ and $\phi_y(z,t)$ are the instantaneous phases of the dominant edgewise and flapwise response as

$$\begin{aligned}\phi_x(z,t) &= \arg\left(\xi_x(z,t) + \mathrm{i}\mathcal{H}(\xi_x(z,t))\right),\\ \phi_y(z,t) &= \arg\left(\xi_y(z,t) + \mathrm{i}\mathcal{H}(\xi_y(z,t))\right),\end{aligned} \tag{15}$$

and $\hat{f}_x(z,t)$ and $\hat{f}_y(z,t)$ represent the instantaneous dominant response frequencies at different spanwise locations obtained based on the local maxima of the wavelet transform magnitude as

$$\hat{f}_x(z,t) = \arg\max_f \left|\mathcal{W}[\xi_x](z,t,f)\right|, \quad \hat{f}_y(z,t) = \arg\max_f \left|\mathcal{W}[\xi_y](z,t,f)\right|, \tag{16}$$

where $\mathcal{W}[-]$ represents the wavelet analysis (Fu et al., 2024) as:

$$\mathcal{W}[\xi] = \left\langle \xi(t), \psi_{a,\tau}(t)\right\rangle = a^{-1/2}\int_{-\infty}^{+\infty} \xi(t)\psi^*\left(\frac{t-\tau}{a}\right)dt, \tag{17}$$

where $\mathcal{W}$ is the wavelet transformation coefficient of the time domain signal $\xi(t)$, which represents the variation in frequency at that time scale. Parameter a is the scale factor, τ is the shift factor, $\psi(t)$ is the mother wavelet, and the Morlet wavelet is chosen as the mother wavelet. All the color gradients shown in the color bar present the normalized data.

For the P80A310 case, the edgewise response is dominated by the second mode, as shown in Fig. 14(a) and (b). In contrast, the flapwise response exhibits two regions that deviate from a pure second-mode response as Fig. 14(c) shows. The first one is at $Z/L \approx 0.76$ and the second one is at $Z/L \in [0, 0.2]$. For the first region, the location is close to the upcrossing zero at $Z/L = 0.72$ as shown in Fig. 11(a), which introduces a first-mode component. In addition, there is higher harmonic component for the response, including $2f_{n2}$ and $3f_{n2}$ harmonic components. This phenomenon is more obvious in the second region, where the $2f_{n2}$ harmonic components dominate the response at $Z/L \approx 0.30$ and $Z/L \approx 0.13$. These two regions are closely associated with the spanwise variation of the phase difference as shown in Fig. 14(d). For the first region, there is an approximately π phase jump in which is related to the zero value of modal shape. This behavior is consistent with flexible pipe VIV (Fan et al., 2019; Fu et al., 2025b), in which phase jumps are

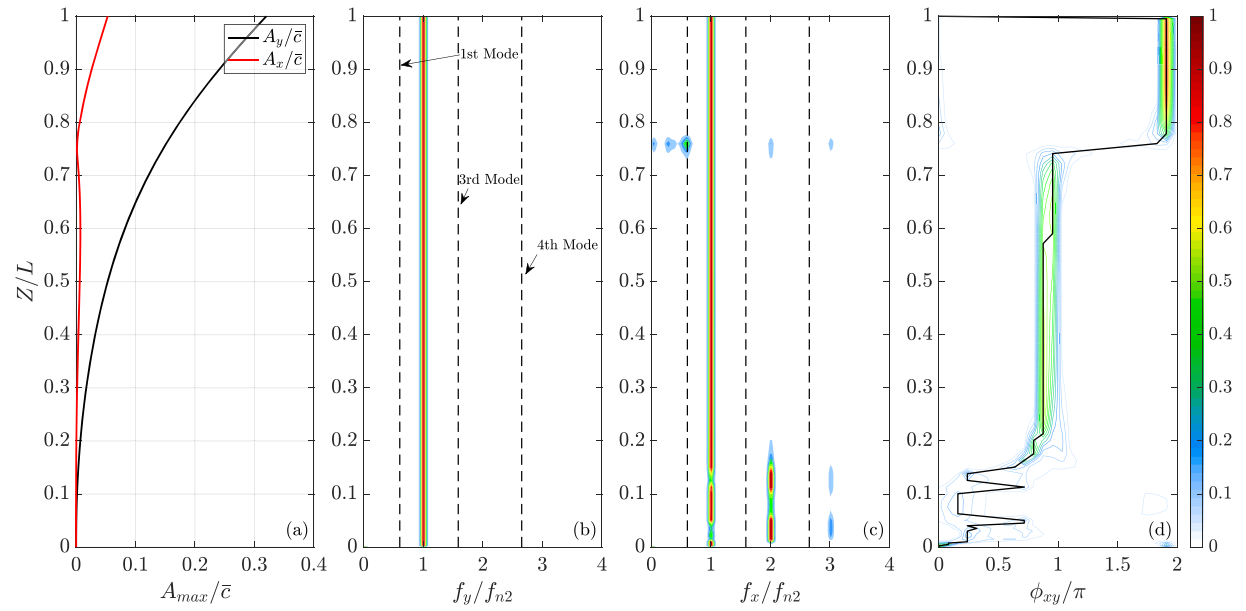

Fig. 14. Spanwise distribution of VIV response for the P80A310 case: (a) nondimensional maximum VIV displacement in flapwise ($A_x/\bar{c}$, red line –) and edgewise ($A_y/\bar{c}$, black line –) directions. The average chord length $\bar{c} = 3.72$ m is used for nondimensionalization. (b) Normalized PSD distribution of spanwise response. The natural frequencies of first, third, and fourth modes are shown with black dashed line (--). (c) Normalized PSD distribution of edgewise response. (d) Histogram of phase difference ϕ_{xy}, where the dominant phase difference is presented in black line (–). The spanwise location is normalized based on blade total length $L = 96.755$ m. (For interpretation of the references to colour in this figure legend, the reader is referred to the web version of this article.)

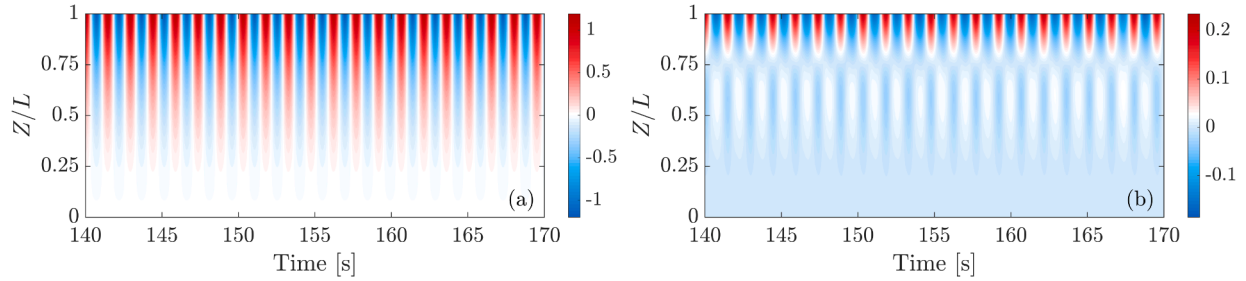

Fig. 15. Spatial and temporal distributions of the VIV displacement along the blade of P80A310 case: (a) edgewise direction and (b) flapwise direction. The unit of displacement contour is meters.

associated with nodes of the in-line mode shape. In the second region, the phase difference is highly irregular and shows no coherent trend. It should be noted that the response amplitude is very low since it is close to the blade root. The mechanism in this region will be investigated in future work.

Fig. 15 shows the traveling wave characteristics of the P80A310 case with the spatial and temporal distribution of the VIV displacement in meters. In this case, VIV is dominated by standing wave behavior. The edgewise response exhibits a consistent vibration pattern, whereas the flapwise response shows little change in the locations of stationary points over time.

Fig. 16 shows the instantaneous VIV response frequency for the P80A310 case obtained via wavelet analysis (Fu et al., 2024) based on Eq. (17). Four spanwise locations are examined: the tip $Z/L = 1.00$; $Z/L = 0.76$ (corresponding to the first deviation region in Fig. 14); $Z/L = 0.44$; and $Z/L = 0.13$ (corresponding to the second deviation region in Fig. 14). For the flapwise response, $Z/L = 1.00$ and $Z/L = 0.44$ exhibit the second-mode-dominated response with a slightly higher harmonic component. The VIV response at $Z/L = 0.76$ presents the mode transition between the first and second modes. The PSD results show the first- and second-mode natural frequencies and the second and third harmonics of the second-mode frequency. The VIV response at $Z/L = 0.13$ is dominated by the second harmonic of the second-mode natural frequency with the third harmonic and the second-mode frequency itself.

Fig. 17 shows the instantaneous wake pattern of P80A310 case at 249 s. The subfigures (a) to (c) on the left show the wake pattern of different spanwise locations corresponding to the black lines. The 2S (two single vortices) wake pattern is shown. The figure on the right shows the vortex shedding of the total blade, which is very chaotic and has a high inclination angle flow. Vortex shedding from the blade exhibits strong three-dimensional effects, and detailed investigations of the VIV mechanism will be conducted in future work.

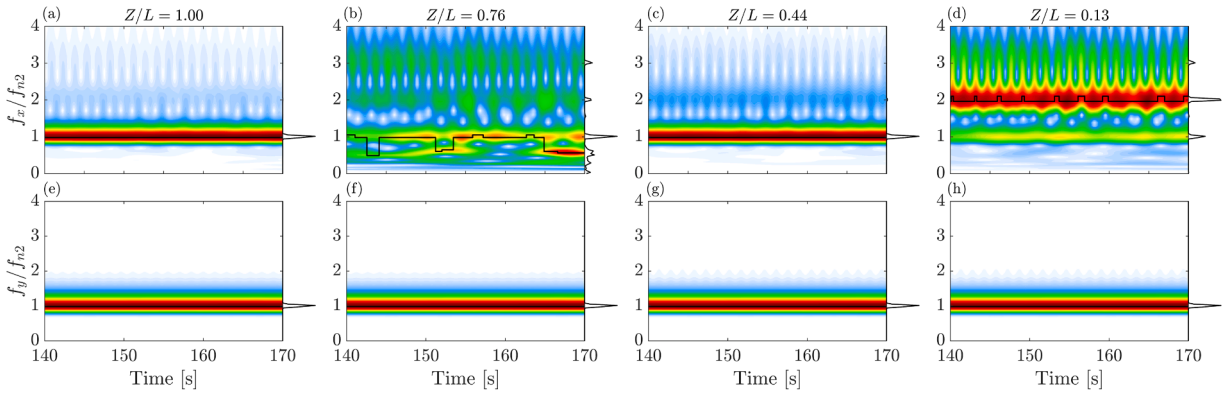

Fig. 16. Time-varying response frequency of P80A310 case by wavelet analysis: (a)–(d) wavelet analysis result of flapwise VIV displacement at location $Z/L = 1.00$, 0.76, 0.44, and 0.13, respectively. (e)–(h) wavelet analysis result of edgewise VIV displacement with the same location of (a) to (d). Black line on the right of each contour represents the corresponding PSD results. Black line in the contour represents the instantaneous dominant frequency by wavelet analysis.

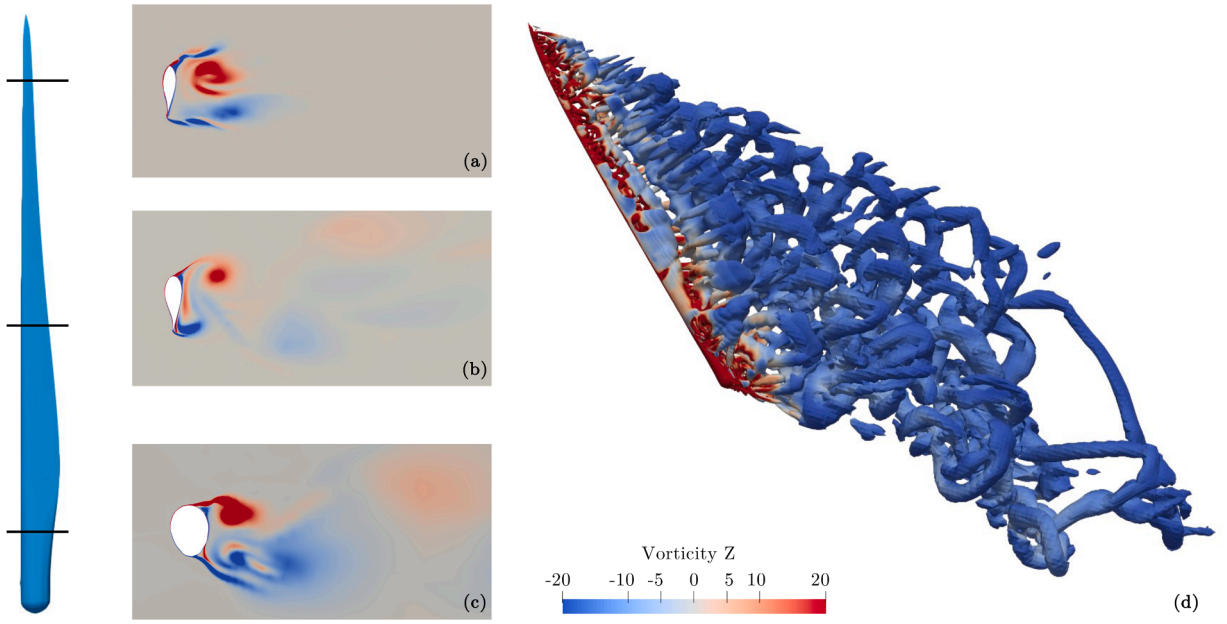

Fig. 17. Wake pattern of blade VIV of P80A310 case at 249 s. (a)–(c) Three slices of near-blade region with vorticity Z contour. The slice locations are indicated by black lines on the blade. (d) Vortex shedding over the full blade.

5.2.2. P95A310 Case

Fig. 18 shows the VIV response for the P95A310 case. Both the edgewise and flapwise responses are also second-mode-dominated, but the first-order region response near $Z/L = 0.76$ is less obvious compared with the P80A310 case in Fig. 14. A π phase jump is still observed, although it is distributed over a broader transition zone of $0.6 < Z/L < 0.8$. The higher harmonic region near root $Z/L \in [0, 0.2]$ shows a similar vibration pattern, two second harmonic regions with chaotic phase difference distribution.

Fig. 19 presents the traveling wave phenomenon for the P95A310 case. The edgewise response still exhibits a strong standing wave pattern, whereas the flapwise response shows a modest traveling wave phenomenon with no clear standing points in the time domain. In both DOFs, the VIV response remains clearly second-mode-dominated.

Fig. 20 shows the instantaneous VIV response frequency for the P95A310 case, obtained via wavelet analysis, at the same four locations as in Fig. 16. The time-varying responses at $Z/L = 1.00$ and $Z/L = 0.44$ are basically the same as for the P80A310 case. The first-order region near $Z/L = 0.76$ shows very limited first-order response in the contour and is more clearly a second-mode-dominated response than in the P80A310 case. There is no obvious mode transition in this case. For the location of $Z/L = 0.13$, the second harmonic is obvious, whereas the third harmonic is very weak in both contour and PSD results.

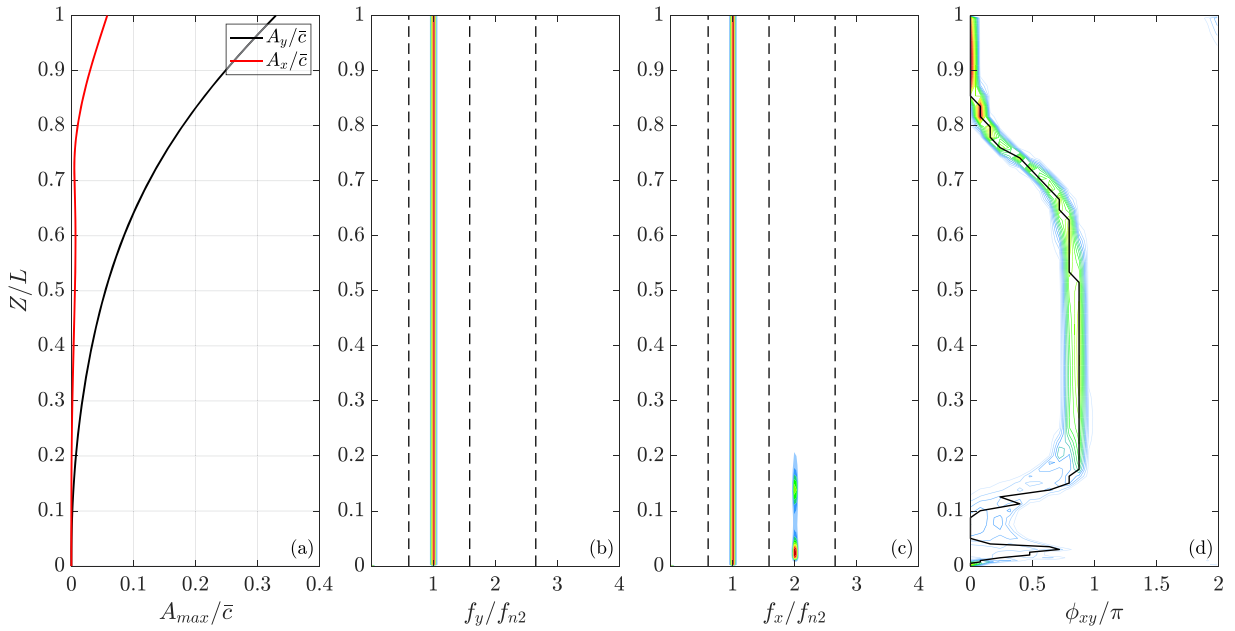

Fig. 18. Spanwise distribution of VIV response for the P95A310 case: (a) Nondimensional maximum VIV displacement in flapwise ($A_x/\bar{c}$, red line –) and edgewise ($A_y/\bar{c}$, black line –) direction. The average chord length $\bar{c}$ = 3.72 m is used for nondimensionalization. (b) Normalized PSD distribution of spanwise response. The natural frequencies of first, third, and fourth modes are shown with black dashed lines (--). (c) Normalized PSD distribution of edgewise response. (d) Histogram of phase difference ϕ_{xy}, where the dominant phase difference is presented with a black line (–). The spanwise location is normalized based on blade total length L = 96.755 m. (For interpretation of the references to colour in this figure legend, the reader is referred to the web version of this article.)

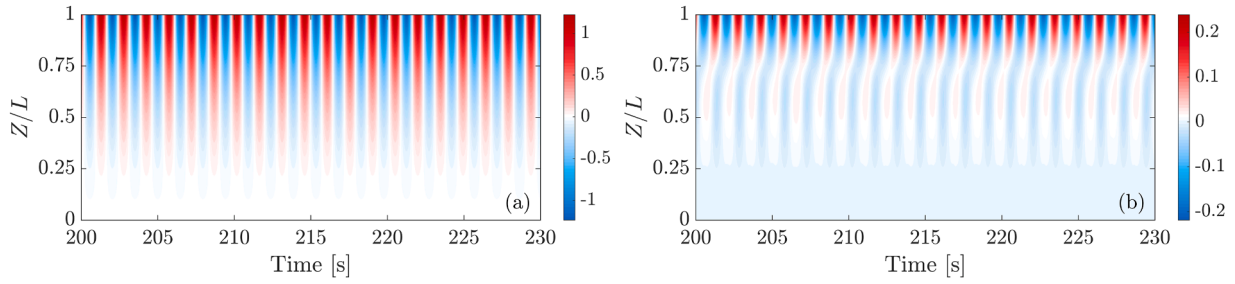

Fig. 19. Spatial and temporal distributions of the VIV displacement along the blade for the P95A310 case: (a) edgewise direction and (b) flapwise direction. The unit of displacement contour is meters.

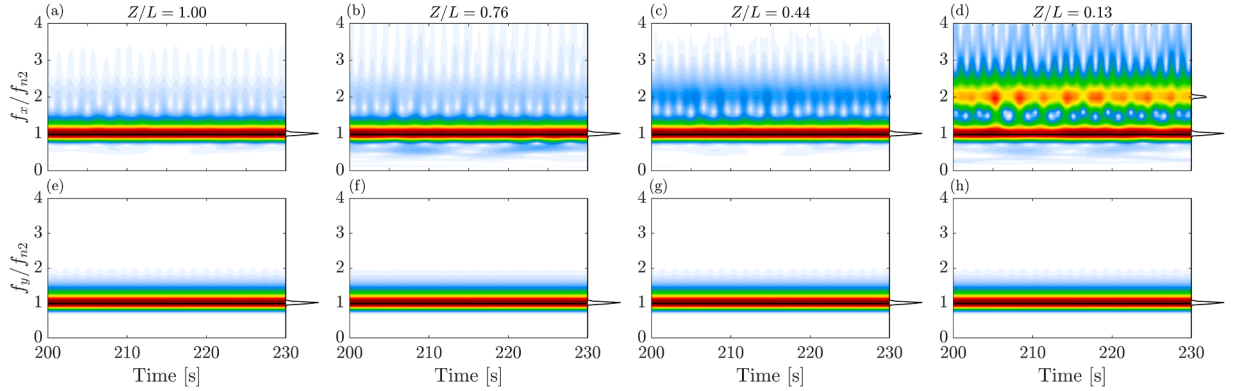

Fig. 20. Time-varying response frequency for the P95A310 case by wavelet analysis: (a)–(d) Wavelet analysis result of flapwise VIV displacement at location Z/L = 1.00, 0.76, 0.44, and 0.13, respectively. (e)–(h) Wavelet analysis result of edgewise VIV displacement with same locations as in (a)–(d). Black line on the right of each contour represents the corresponding PSD results. Black line in the contour represents the instantaneous dominant frequency by wavelet analysis.

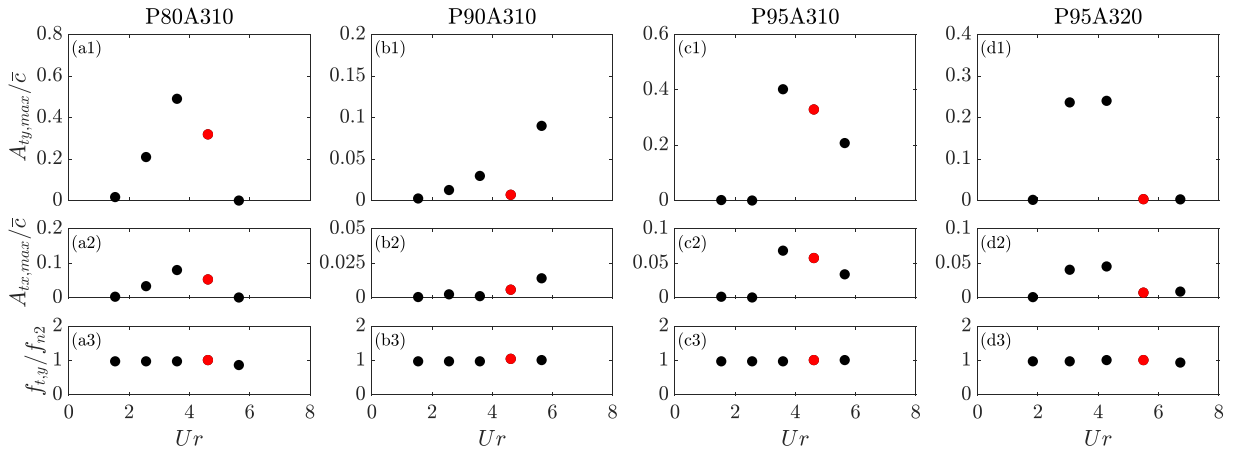

Fig. 21. VIV response of tip structure versus reduced velocity: (a1)–(d1) Maximum nondimensional tip edgewise VIV response for the P80A310, P90A310, P95A310, and P95A320 cases, respectively. (a2)–(d2) Maximum nondimensional tip flapwise VIV response of corresponding cases. (a3)–(d3) Nondimensional edgewise VIV frequency corresponding cases. The red dots are the results shown in previous section. (For interpretation of the references to colour in this figure legend, the reader is referred to the web version of this article.)

5.3. Reduced velocity effect

Blade VIV exhibits the response with significant single-mode dominance. For the single-mode-dominated VIV, reduced velocity Ur is one of the key VIV mechanism parameters. Reduced velocity Ur in the present study is defined as:

$$Ur = \frac{U\cos\gamma}{f_{n2}\bar{c}}, \tag{18}$$

where U is fixed incoming flow velocity, γ is the azimuth rotation angle defined in Fig. 1, f_{n2} is the second-mode (first edgewise mode) natural frequency, and $\bar{c}$ is the mean chord length. It should be noted that independence principle (Jain and Modarres-Sadeghi, 2013) is applied in these highly inclined angle flow cases where it is not strictly appropriate. Given that this is an early-stage analysis of blade VIV, we employ it only as a reduced velocity approximation.

Fig. 21 presents the VIV response as a function of reduced velocity for four configurations across five incoming flow speeds: $U = 6\,\text{m/s}$, $10\,\text{m/s}$, $14\,\text{m/s}$, $18\,\text{m/s}$, and $22\,\text{m/s}$. The flow direction and blade configuration are kept constant, with only the incoming flow velocity varied. The time step is set to $0.0025\,\text{s}$ for cases with $U < 18\,\text{m/s}$, whereas for the $U = 22\,\text{m/s}$ case the time step is $0.002\,\text{s}$. The red dots in the figure denote the cases presented in the previous section. It can be seen that the VIV response exhibits large variance with respect to flow velocity and does not follow a linear trend. In particular, the configuration that showed only limited VIV in the previous study (Horcas et al., 2022b) can develop significant VIV at even lower flow velocities, as illustrated in Fig. 21(d).

The blade VIV shows a two-branch development pattern similar to that of the high-mass-ratio bluff cylinder VIV with an initial branch and a lower branch (Williamson and Govardhan, 2004). In the initial branch, the VIV amplitude increases with increasing reduced velocity, and the amplitude decreases as the reduced velocity increases in the lower branch. Using the P80A310 case as an example, the initial branch is about $0 < Ur < 4$, and the lower branch is about $4 < Ur < 8$. P95A310 and P95A320 exhibit VIV development patterns similar to P80A310. For P90A310, the VIV amplitude increases near $Ur \approx 6$. Additional cases will be examined in future work.

Meanwhile, the flapwise response exhibits the same trend as the edgewise response, which is also the case with the bluff cylinder VIV (Fu et al., 2025a). The VIV frequency is locked in the second-mode natural frequency for all cases; there is no desynchronization region in the present study.

6. Conclusions and future work

This work presented the first open-source three-dimensional simulations of VIV of a single prototype IEA 10-MW reference blade of length $97.325\,\text{m}$ using the ExaWind stack. The main purposes for the present study were to 1) provide systematic verification results for the ExaWind-based blade VIV results, with mesh and time step studies and a practical comparison of VIV triggering strategies, and 2) provide the main blade VIV spanwise response characteristics with an analysis of varied configuration and flow conditions. The principal conclusions are:

1) Five near-body surface meshes (C385S317, C385S662, C385S1001, C513S317, C513S662) were assessed at $\Delta t = 0.0025\,\text{s}$, and a time step study ($\Delta t = \{0.005,\ 0.0025,\ 0.001\}\,\text{s}$) was performed on C385S662. Peak tip responses for the strongly excited cases (P80A310, P95A310) varied by 5 to 10% across meshes and were nearly unchanged between $\Delta t = 0.0025\,\text{s}$ and $0.001\,\text{s}$, indicating mesh and time step sufficiency for the present scope. C385S662 with $\Delta t = 0.0025\,\text{s}$ was adopted for production runs as a balance of accuracy and cost.

2) Five practical VIV triggering strategies (no forcing; three linear ramps of increasing magnitude; one harmonic forcing) produced indistinguishable fully developed VIV amplitudes for a given inflow condition. Stronger ramps/harmonic forcing shorten the spin-up time substantially; a linear ramping procedure with 8×10^3 N was adopted.

3) The blade VIV response was dominated by the first edgewise (second overall) mode. Minor contributions from the first mode appear locally where the second-mode shape crosses zero along the span with mode transition. Rotational DOFs remain small compared with translational motion. There is no obvious traveling phenomenon in the present study.

4) Across four configurations and five inflow speeds, the tip response versus reduced velocity Ur displayed the classical two-branch behavior (growth with Ur in the initial branch, decay in the lower branch). Within the sampled range, the dominant VIV frequency remained locked to the second-mode natural frequency and no desynchronization was observed.

Overall, the results demonstrated that pronounced VIV responses, with tip displacements on the order of 1 m, can occur under specific configurations and flow conditions. Moreover, a configuration that yields no VIV (Horcas et al., 2022b) in one flow case can develop significant VIV when the flow velocity changes. These findings indicate the increasing potential for VIV fatigue damage, which requires attention during operation.

The setup for all cases is hosted in the ExaWind GitHub repository and is open source for the community. In this paper, we focus on the VIV response characteristics of the wind turbine blade. Using the ExaWind framework, the detailed further VIV mechanism studies, including VIV mean drag properties, excitation mechanism and energy input-output analysis, will be conducted as future work. Meanwhile, to our best knowledge, there are currently no publicly available experimental data on VIV of wind turbine blades or rotors at either full scale or reduced scale in the wind energy field. To improve the credibility of the simulation results, the experiment of the prototype blade VIV is being planned, and corresponding validation activities will also be carried out.

CRediT authorship contribution statement

Xuepeng Fu: Writing – review & editing, Writing – original draft, Investigation, Formal analysis, Data curation, Conceptualization; **Ganesh Vijayakumar:** Writing – review & editing, Project administration, Investigation, Conceptualization; **Bumseok Lee:** Writing – review & editing, Writing – original draft, Investigation; **Michael Sprague:** Writing – review & editing, Project administration, Funding acquisition.

Data Availability

The ExaWind configuration used in this study is open source and available in the ExaWind GitHub repository at https://github.com/Exawind/exawind-benchmarks.

Declaration of interests

The authors declare that they have no known competing financial interests or personal relationships that could have appeared to influence the work reported in this paper.

Acknowledgments

This work was authored by the National Laboratory of the Rockies for the U.S. Department of Energy (DOE), operated under Contract No. DE-AC36-08GO28308. Funding provided by the U.S. Department of Energy Office of Energy Efficiency and Renewable Energy Wind Energy Technologies Office. The views expressed in the article do not necessarily represent the views of the DOE or the U.S. Government. The U.S. Government retains and the publisher, by accepting the article for publication, acknowledges that the U.S. Government retains a nonexclusive, paid-up, irrevocable, worldwide license to publish or reproduce the published form of this work, or allow others to do so, for U.S. Government purposes. The research was performed using computational resources sponsored by the U.S. Department of Energy's Office of Energy Efficiency and Renewable Energy and located at the National Laboratory of the Rockies. The authors gratefully acknowledge Prof. Niels Nørmark Sørensen at the Technical University of Denmark for providing the data and meshes, and for valuable discussions. The authors also thank Dr. Martin Stettner, GE Vernova for valuable discussions.

References

Bauchau, O.A., 2011. Flexible multibody dynamics. Vol. 176. Springer.

Bidadi, S., Vijayakumar, G., Lee, B., Sprague, M., 2025. Freestream turbulence effects on unsteady wind turbine loads and wakes: an IDDES study. J. Wind Eng. Ind. Aerodyn. 267, 106211.

Bidadi, S., Vijayakumar, G., Sharma, A., Sprague, M., 2023. Mesh and model requirements for capturing deep-stall aerodynamics in low-mach-number flows. J. Turbul. 24 (8), 393–418.

Bortolotti, P., Tarres, H.C., Dykes, K., Merz, K., Sethuraman, L., Verelst, D., Zahle, F., 2019. IEA Wind Task 37 on Systems Engineering in Wind Energy – WP2.1 Reference Wind Turbines. Technical Report. International Energy Agency. https://www.nrel.gov/docs/fy19osti/73492.pdf.

Bourguet, R., Karniadakis, G.E., Triantafyllou, M.S., 2013. Distributed lock-in drives broadband vortex-induced vibrations of a long flexible cylinder in shear flow. J. Fluid Mech. 717, 361–375.

Duan, J., Zhou, J., You, Y., Wang, X., 2021. Effect of internal flow on vortex-induced vibration dynamics of a flexible mining riser in external shear current. Mar. Struct. 80, 103094.

Falgout, R.D., Yang, U.M., 2002. Hypre: a library of high performance preconditioners. In: Computational Science — ICCS 2002. Springer Berlin Heidelberg, Berlin, Heidelberg, pp. 632–641. https://doi.org/10.1007/3-540-47789-6_66

Fan, D., Wang, Z., Triantafyllou, M.S., Karniadakis, G.E., 2019. Mapping the properties of the vortex-induced vibrations of flexible cylinders in uniform oncoming flow. J. Fluid Mech. 881, 815–858.
Feng, C.C., 1968. The measurement of vortex induced effects in flow past stationary and oscillating circular and D-section cylinders. Ph.D. thesis. University of British Columbia. Vancouver.
Fu, X., Fu, S., Han, Z., Niu, Z., Zhang, M., Zhao, B., 2025a. Numerical simulations of 2-DOF vortex-induced vibration of a circular cylinder in two and three dimensions: a comparison study. J. Ocean Eng. Sci. 10 (4), 395–410.
Fu, X., Fu, S., Niu, Z., Zhao, B., Shen, J., Deng, P., 2025b. A validated fluid-structure interaction simulation model for vortex-induced vibration of a flexible pipe in steady flow. Mar. Struct. 104, 103895.
Fu, X., Fu, S., Ren, H., Xie, W., Xu, Y., Zhang, M., Liu, Z., Meng, S., 2022a. Experimental investigation of vortex-induced vibration of a flexible pipe in bidirectionally sheared flow. J. Fluids Struct. 114, 103722.
Fu, X., Fu, S., Zhang, M., Ren, H., Zhao, B., Xu, Y., 2024. Vortex-induced vibration of a flexible pipe under oscillatory sheared flow. Phys. Rev. Fluids 9 (1), 014604.
Fu, X., Zhang, M., Fu, S., Zhao, B., Ren, H., Xu, Y., 2022b. On the study of vortex-induced vibration of a straked pipe in bidirectionally sheared flow. Ocean Eng. 266, 112945.
Govardhan, R., Williamson, C., 2002. Resonance forever: existence of a critical mass and an infinite regime of resonance in vortex-induced vibration. J. Fluid Mech. 473, 147–166.
Govardhan, R., Williamson, C.H.K., 2000. Modes of vortex formation and frequency response of a freely vibrating cylinder. J. Fluid Mech. 420, 85–130.
Grinderslev, C., Houtin-Mongrolle, F., Nørmark Sørensen, N., Raimund Pirrung, G., Jacobs, P., Ahmed, A., Duboc, B., 2023. Forced motion simulations of vortex-induced vibrations of wind turbine blades–a study of sensitivities. Wind Energy Sci. Discuss. 2023, 1–23.
Grinderslev, C., Nørmark Sørensen, N., Raimund Pirrung, G., González Horcas, S., 2022. Multiple limit cycle amplitudes in high-fidelity predictions of standstill wind turbine blade vibrations. Wind Energy Sci. 7 (6), 2201–2213.
Gritskevich, M.S., Garbaruk, A.V., Schütze, J., Menter, F.R., 2012. Development of DDES and IDDES formulations for the $k-\omega$ shear stress transport model. Flow, Turbul. Combust. 88, 431–449.
Heinz, J.C., Sørensen, N.N., Zahle, F., Skrzypiński, W., 2016. Vortex-induced vibrations on a modern wind turbine blade. Wind Energy 19 (11), 2041–2051.
Horcas, S.G., Barlas, T., Zahle, F., Sørensen, N.N., 2020. Vortex induced vibrations of wind turbine blades: influence of the tip geometry. Phys. Fluids 32 (6).
Horcas, S.G., Madsen, M. H.A., Sørensen, N.N., Zahle, F., Barlas, T., 2022a. Influence of the installation of a trailing edge flap on the vortex induced vibrations of a wind turbine blade. J. Wind Eng. Ind. Aerodyn. 229, 105118.
Horcas, S.G., Sørensen, N.N., Zahle, F., Pirrung, G.R., Barlas, T., 2022b. Vibrations of wind turbine blades in standstill: mapping the influence of the inflow angles. Phys. Fluids 34 (5).
Huera-Huarte, F.J., 2006. Multi-mode vortex-induced vibrations of a flexible circular cylinder. Ph.D. thesis. University of London.
Huera-Huarte, F.J., 2025. Vortex-induced vibration of flexible cylinders in cross-flow. Annu. Rev. Fluid Mech. 57, 285–310.
Jain, A., Modarres-Sadeghi, Y., 2013. Vortex-induced vibrations of a flexibly-mounted inclined cylinder. J. Fluids Struct. 43, 28–40.
Jonkman, B., Platt, A., Mudafort, R.M., Branlard, E., Wang, L., Slaughter, D., Sprague, M., Ross, H., Jonkman, J., Chetan, M., Davies, R., Hall, M., Vijayakumar, G., Buhl, M., Bortolotti, P., Ashesh, S., 2025. OpenFAST v4.0.2. https://doi.org/10.5281/zenodo.14847846.
Jonkman, J.M., Wright, A.D., Hayman, G.J., Robertson, A.N., 2018. Full-system linearization for floating offshore wind turbines in openFAST. In: International Conference on Offshore Mechanics and Arctic Engineering. Vol. 51975. American Society of Mechanical Engineers, p. V001T01A028.
Khalak, A., Williamson, C.H.K., 1999. Motions, forces and mode transitions in vortex-induced vibrations at low mass-damping. J. Fluid Mech. 13 (7–8), 813–851.
Kuhn, M.B., Henry de Frahan, M.T., Mohan, P., Deskos, G., Churchfield, M., Cheung, L., Sharma, A., Almgren, A., Ananthan, S., Brazell, M.J., Martínez-Tossas, L.A., Thedin, R., Rood, J., Sakievich, P., Vijayakumar, G., Zhang, W., Sprague, M., 2025. Amr-wind: a performance-portable, high-fidelity flow solver for wind farm simulations. Wind Energy 28 (5), e70010.
Livanos, D., 2018. Investigation of vortex induced vibrations on wind turbine towers. Master's thesis. Delft University of Technology.
Sarpkaya, T., 2004. A critical review of the intrinsic nature of vortex-induced vibrations. J. Fluids Struct. 19 (4), 389–447.
Secco, N., Kenway, G. K.W., He, P., Mader, C.A., Martins, J. R.R.A., 2021. Efficient mesh generation and deformation for aerodynamic shape optimization. AIAA J. . https://doi.org/10.2514/1.J059491
Sharma, A., Brazell, M.J., Vijayakumar, G., Ananthan, S., Cheung, L., deVelder, N., Henry de Frahan, M.T., Matula, N., Mullowney, P., Rood, J., Sakievich, P., Almgren, A., Crozier, P.S., Sprague, M., 2024. Exawind: open-source CFD for hybrid-RANS/LES geometry-resolved wind turbine simulations in atmospheric flows. Wind Energy 27 (3), 225–257.
Shen, J., Fu, S., Fu, X., Moan, T., Sævik, S., 2025. Flow-induced vibration of twin-pipe model with varying mass and damping: a study using virtual physical framework. J. Fluids Struct. 139, 104438.
Sprague, M.A., Ananthan, S., Vijayakumar, G., Robinson, M., 2020. Exawind: a multifidelity modeling and simulation environment for wind energy. J. Phys. Conf. Ser. 1452 (1), 012071.
Swithenbank, S.B., Larsen, C.M., 2012. Occurrence of high amplitude VIV with time sharing. In: International Conference on Offshore Mechanics and Arctic Engineering. Vol. 44922. American Society of Mechanical Engineers, pp. 723–729.
Wang, Q., Sprague, M.A., Jonkman, J.M., 2016. Partitioned nonlinear structural analysis of wind turbines using beamdyn. In: 34Th Wind Energy Symposium, p. 0753.
Willden, R.H.J., Graham, J.M.R., 2001. Numerical prediction of VIV on long flexible circular cylinders. J. Fluids Struct. 15 (3–4), 659–669.
Williamson, C.H.K., Govardhan, R., 2004. Vortex-induced vibrations. Annu. Rev. Fluid Mech. 36 (1), 413–455.
Williamson, C.H.K., Govardhan, R., 2008. A brief review of recent results in vortex-induced vibrations. J. Wind Eng. Ind. Aerodyn. 96 (6–7), 713–735.
Xu, K., Bi, K., Han, Q., Li, X., Du, X., 2019. Using tuned mass damper inerter to mitigate vortex-induced vibration of long-span bridges: analytical study. Eng. Struct. 182, 101–111.
Zhang, W., Almgren, A., Beckner, V., Bell, J., Blaschke, J., Chan, C., Day, M., Friesen, B., Gott, K., Graves, D., Katz, M., Myers, A., Nguyen, T., Nonaka, A., Rosso, M., Williams, S., Zingale, M., 2019. AMReX: a framework for block-structured adaptive mesh refinement. J. Open Source Soft. 4 (37), 1370.
Zhao, B., Fu, S., Deng, P., Zhang, M., Bai, Y., Fu, X., 2024. Frequency-domain prediction method for vortex/wake-induced vibrations of double flexible risers in tandem arrangements. Ocean Eng. 297, 116942.
Zhao, B., Zhang, M., Fu, S., Fu, X., Sun, T., Song, B., 2023. Experimental investigation on vortex/wake-induced force of double unequal-diameter flexible cylinders in tandem. Phys. Fluids 35 (5).